Escola de Camins
Escola Tècnica Superior d'Enginyeria de Camins, Canals i Ports
UPC BARCELONATECH

MASTER THESIS - MASTER ON NUMERICAL METHODS IN ENGINEERING

NUMERICAL MODELLING OF RAILWAY BALLAST USING THE DISCRETE ELEMENT METHOD

Author:
Joaquín Irazábal González

Tutors:
Eugenio Oñate Ibáñez de Navarra
Fernando Salazar González

Date:
29 June 2015

Contents

List of Figures

List of tables

Abstract

The development of high-speed train lines has increased during the last twenty years, leading to more demanding loads in railway infrastructures. For these reasons, a discrete element model of granular material was carried out using 3D spherical particles with a rolling resistance, in order to consider non-sphericity of ballast stones. Other discrete element model representing granular materials as sphere aggregates (sphere clusters) has been also implemented. Current work presents the methodology followed to develop the discrete element model able to calculate railway ballast interaction. Interaction between discrete and finite elements is another key point of the calculations that is addressed. This document displays some results evaluating the influence of material parameters and geometric representation in the simulation of railway ballast and presents some laboratory tests calculated with the numerical application developed.

1 INTRODUCTION

The railway track system plays an important role in the transport network of any country, and its maintenance is essential. Before the advent of high-speed train lines, most attention has been given to the track superstructure consisting of rails, fasteners and sleepers, and less attention has been given to the substructure consisting of ballast, subballast and subgrade. However, the maintenance cost of the substructure is not negligible at all and should be taken into account [56].

1.1 Motivation

Besides the importance of the study of ballast properties, in economic terms, it should be pointed that a new variable appeared in the last two decades: the increase of trains speed. This new way of transport, which has improved people mobility all around the world, is also more demanding in terms of loads and vibrations [34].

One of the main problems that has appeared with the increase of train speed is, the so-called, *ballast flight*. The traditional ballasted track is certainly a good solution, both technically and economically. However, the high-speed air fluxes generated by the train, passing at certain velocity, can cause movement of ballast particles. Those particles can hit the underbody of the train, they can be crushed by the wheels against the rail (damaging both elements) or they can be projected laterally outside the railroad. If those stones bounce off causing the release of other particles they could generate a phenomenon called *ballast clouds*.

Figure 1.1: High-speed train travelling over a ballast railway track.

A possible solution to this problem is to reduce the thickness of the ballast bed, in order to increase the space between train and ballast, that will lead to the decrease of the air speed fluxes. This solution leaves the sleeper slightly uncovered, which can cause new problems like excessive settlements and horizontal displacements in some sections.

Everything above mentioned suggests that a deep study of this infrastructure must be carried out, and here is where numerical methods become important.

Refined constitutive models, based on continuum assumptions, are generally used to investigate many complex geomechanic problems. These models result in powerful tools to describe the critical states for soils, although they do not represent the local discontinuous nature of the material [16], [17]. However, discontinuities play a major role in the behaviour of granular materials inducing special features such as anisotropy or local instabilities, which are difficult to understand or model based on the principles of continuum mechanics.

The discrete element method (DEM) is an alternative approach, that considers the granular nature of the material and provides a new insight in the constitutive model. In it, the material is modelled particle by particle and interaction between those particles determine material response [7]. DEM has proven to be a very useful tool to obtain complete qualitative information on calculations of groups of particles [30].

Current work objective is to reproduce quantitatively the macro-mechanical behaviour of railway ballast, based in DEM. To that end, some laboratory tests are reproduced using a simple DEM formulation. From the point of view of micro-scale analysis, it is essential to represent the exact geometry of the particle. On the other hand, if the interest lies in the behaviour of the granular material as a whole, it is thought that the geometry of each particle is not a determining factor. For that reason two different approaches, one using spheres to represent particles and other using particles more similar to real ones (their definition will be explained in advanced in section 3.2.2), will be studied. The use of spheres is a very efficient approach in terms of computational cost, but it could be a very rough simplification.

The main material contact parameters, to be defined in the numerical model are: normal contact stiffness, tangential contact stiffness, local friction, restitution coefficient and, if particles are modelled as spheres, rolling friction coefficient, which is a dimensionless parameter that controls the limit of rolling (it is necessary due to the fact that the interest is in simulating a material with irregular shape). Normal and tangential contact stiffness can be derived from material Young and Poisson coefficients.

The numerical discrete element model, for the simulation of ballast aggregates, has been implemented in *Kratos*, a multidisciplinary framework for the development of finite and discrete element programs (that is being developed by CIMNE[1]), within an application called *DEM-application*, [15], [53], [54].

[1]Centre Internacional de Mètodes Numèrics en Enginyeria.

1.2 Objectives and outline

This work is part of the research project *Modelación numérica del conjunto carril-traviesa-balasto mediante el Método de los Elementos Discretos (BALAMED)*[2] carried out in CIMNE.

The main objective of this thesis is the development of a Discrete Element Model to reproduce railway ballast behaviour. To achieve this objective, the scheme followed is:

- Chapter 2 introduces the literature review. The first part of the chapter is based in railroad infrastructures, train load imposition and ballast properties. The aim is to have as much information as possible to define the simulations in the most accurate manner. Then, in the second part, the DEM is presented, including constitutive models, force calculation, time integration, neighbour search and coupling with the Finite Element Method (FEM).
- Chapter 3 shows code contributions developed in this work: rolling friction implementation, sphere clusters generation and improvements in the discrete-finite element contact detection.
- Chapter 4 presents two laboratory tests used to calibrate and validate the method. The first one was the evaluation of ballast lateral resistance against sleeper movement and the second one a large-scale triaxial test. The definition of the geometry, mesh and initial conditions of the simulations representing those laboratory tests is also displayed.
- Chapter 5 shows the results obtained with *Kratos* using the *DEM-application* and the comparison with laboratory results. Those results comparison led to: material parameters calibration and validation of code improvements.
- Finally, chapter 6 and 7 present the conclusions and future work respectively.

[2]Project financed by Spanish Government with reference number: BIA2012-39172

2 LITERATURE REVIEW

This chapter is divided in two sections. The first section presents a brief introduction of railway structures and a review of its components, from the superstructure, consisting on sleeper, rail and fasteners, to the infrastructure, focusing on ballast. Moreover, section 2.2 introduces the DEM as a general approach for the calculation of granular materials.

2.1 Introduction to railway structures

The railway structure can be split in two parts; the infrastructure, whose main objective is the distribution of the train loads to the soil, and the superstructure, whose aim is the transmission of the train loads to the infrastructure. The superstructure is directly in contact with train wheels.

2.1.1 Railway infrastructure

Traditionally, the conventional railway infrastructure cross-section configuration consist in a simple ballast layer over the platform. Besides distributing traffic loads, the ballast layer contributes to rainwater evacuation, platform protection to moisture variance, longitudinal and lateral stabilization and high loads damping [12].

However, due to the more demanding loads, for high-speed lines, there are several layers of different materials over the platform. The difference between conventional and high-speed train lines cross-section can be seen in Figure 2.1(a).

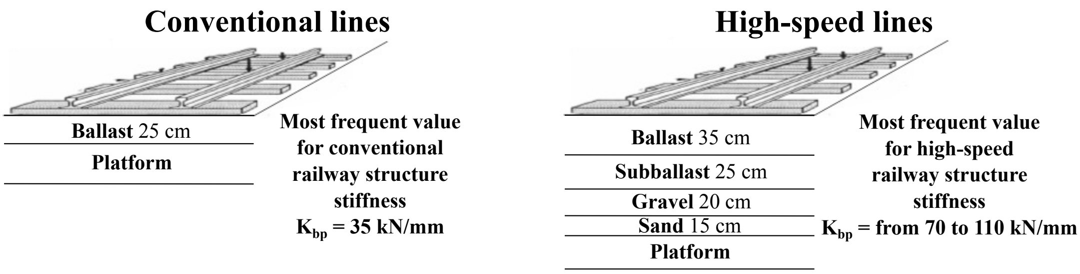

(a) Conventional railway structure. (b) High-speed train railway structure.

Figure 2.1: Convetional and high-speed railway substructure scheme. Typical values for the vertical stiffness of the platform and subgrades (K_{bp}). Source: López Pita [36].

Each layer characteristics are [36]:

- Ballast: the top layer of granular material, about 35 cm thick, which is directly in contact with the sleepers. It mainly helps to bear and damp the train loads transmitted from the railroad sleepers. It also facilitate water drainage.
- Subballast: layer composed by a mixture of ballast, gravel and sand located immediately below ballast and over the platform. Its main functions are the prevention of platform damage due to erosion, rainwater drain and load distribution.
- Platform: the basis for the railway infrastructure.

2.1.2 Railway superstructure

The other main part of the railroad is the superstructure which components are [36]:

- Rail: it is directly responsible of supporting the vehicles passing. Its weight is about 60 kg/m.
- Fasteners: there are different types. It is the element that fixes the rails to the sleepers. There are four per sleeper, which corresponds to two per rail.
- Bearing plate: an elastic pad between the sleeper and the rail that provides greater vertical elasticity to the whole structure.

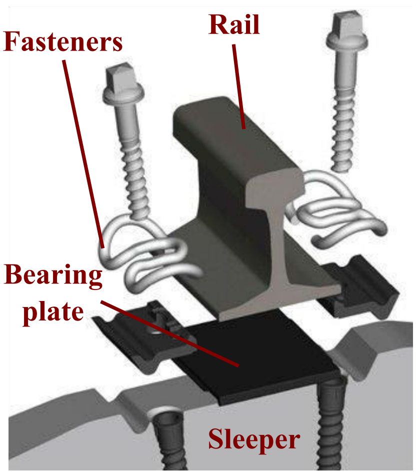

Figure 2.2: Superstructure configuration.

Other components

In addition to the main components shown in Figure 2.2, there are two other significant elements that form the superstructure of the track:

- Rubber sole: an elastic element located under the sleepers to modify track stiffness and increase elasticity. It is normally used in viaducts where track elasticity should be reduced in order to reduce its rapid damage.

- Resilient pad: placed under the ballast in order to change track stiffness and elasticity. It has a similar use as the rubber soles.

2.1.3 Railway geometrical quality

When a train travels over the track, it has six degrees of freedom, three corresponding to displacement: longitudinal (travelling direction), vertical and lateral, and the other three corresponding to rotations about those axes which are called: roll (about the longitudinal axis), yaw (about the vertical axis) and pitch (about the lateral axis). Figure 2.3 shows a diagram of those movements.

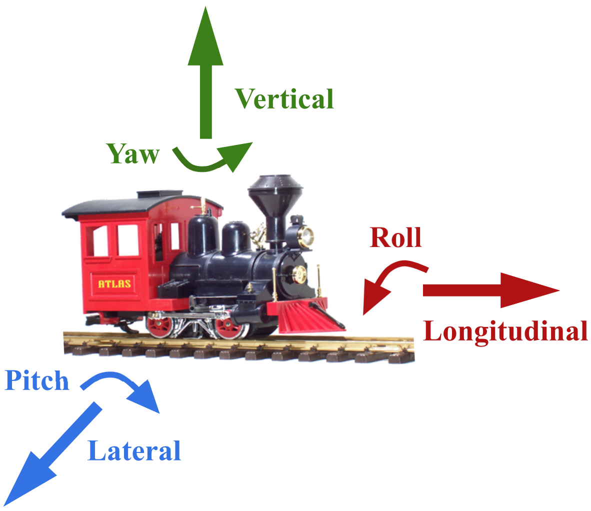

Figure 2.3: Train displacements and rotations designation. The vehicle travels in the longitudinal direction.

These displacements and rotations produce a set of loads that have to be taken into account for dimensioning the railway track. Vertical loads are the main criteria for designing the components of the track, lateral loads determine the maximum speed of vehicles movement, whereas longitudinal loads can cause horizontal buckling of the track.

Track quality can be quantified by the following parameters [20]:

- Vertical alignment: this parameter defines the variations in height of the rail upper surface, relative to a reference plane.
- Cross level: this parameter sets the difference in height between the upper surface of both rails on a section normal to the axis of the road.
- Track gauge: parameter determining the distance between the active faces of the heads of the rails 14 mm below the rolling surface.
- Horizontal alignment: parameter which, for each rail, represents the distance, from above, compared to the theoretical alignment.
- Track twist: represents the distance between a point of the track and the plane formed by three points belonging to the same railway. It has an impact on possible derailments.

Figure 2.4 shows schematically some of these defects.

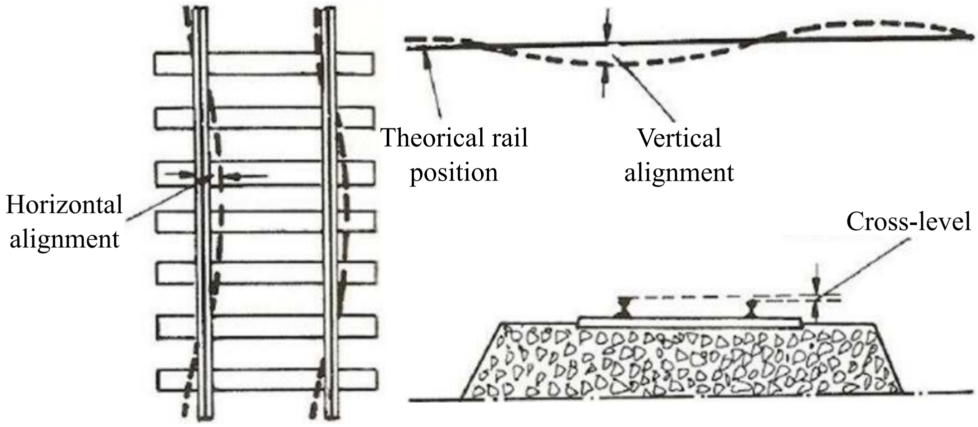

Figure 2.4: Typical railway track alignment defects. Source: López Pita [36].

The quantification of these parameters allows to determine the railway track quality in terms of safety and comfort. Therefore, during construction and conservation, each railway manager requires maximum tolerances for each one of these five factors.

2.1.4 Railway stiffness

Railway stiffness refers to the vertical stiffness of the whole structure [56]. Burrow [11] highlighted that the magnitude of the track stiffness is mainly influenced by the infrastructure, composed by ballast, subballast and platform. Considering only these settlement layers, the ballast is the most relevant material. Comparatively, the platform influences more, but its stiffness is almost imposed.

As Burrow developed [11], there is an optimal track stiffness (at least from the theoretical point of view). When track stiffness is excessively low, too much rail deformation may occur, while, if track stiffness is high, the railroad would be damaged rapidly. López Pita et al. [37] proposed a range of optimal values for vertical stiffness. Their work was based on optimizing maintenance costs and energy dissipation costs (due to excessive deformations), depending on track stiffness. They used data from the high-speed lines Paris-Lyon and Madrid-Sevilla. The study concluded that the track stiffness must be between 70 and 80 kN/mm.

The EUROBALT II European project also dealt with the deterioration of railway tracks. Its main objective was to identify the parameters that should be controlled to reduce damage in railway tracks. The findings of this study were that the most influencing parameters to the track behaviour were: the stiffness, the displacement of the rails and the settlement of the different layers.

2.1.5 Ballast and sleepers

In the next paragraphs, the main features and properties of ballast and sleepers are presented. Firstly, railway ballast properties are described, as its study is the objective of this work. Then, the main features of sleepers used in Spain are defined. Sleepers are significant because they directly interact with ballast.

Ballast specifications

Ballast, as structural element, is formed by a set of particles of different size and shape. The ballast is, thus, a layer of granular material which is placed under the sleepers and therefore develops an important role: resisting to vertical and horizontal loads, produced by the passing train over the rail, and facing climate action.

European Standard EN 13450 specifies the technical characteristics of ballast, used as a supporting layer, in railway tracks. The Standard defines quality controls to which ballast should be subjected.

The Standard uses five properties of aggregates to define the specifications of ballast used in railway tracks: granulometry, Los Angeles coefficient (CLA)[3], micro-Deval coefficient (MDS)[4], flakiness index and particle length.

The size distribution of particles established by the European Standard EN 13450 is presented in Table 2.1.

Table 2.1: Ballast granulometry. Source: CENIT [12].

Sieve size (mm)	cumulative % passing through each sieve
63	100
50	70-100
40	30-65
31,5	0-25
22,4	0-3
32-50	≥ 50

Table 2.1 shows that particle size should be between about 20 and 60 mm. Moreover, the aim is to avoid the presence of angular particles, because they can obstruct tamping operation and they have tendency to slip. In order to resist tamping, a hard enough rock, difficult to break, is needed. According to the Spanish Railway Standard of 2000, this requirement is met if the original rock has a compression resistance of 1200 kg/cm^2.

Tamping operation is necessary because when a vehicle is travelling trough the railway track two different phenomenon appear simultaneously [3]:

- Vertical deflection: affects a rail length of 3 to 4 meters approximately. Its maximum value in the point of application of the load ranges from 1.5 to 2 mm, considering a load of 10 tons per wheel.

[3]Wear coefficient of Los Angeles (CLA). It measures wear resistance by attrition and impact of aggregates. It is the ratio of the difference in weight of the initial sample and the material retained by the sieve 1.6 mm UNE (once subjected to an abrasive and standardized process using iron balls), divided by the initial weight of the sample.

[4]Deval coefficient: determined by the value obtained in the Deval test, consisting of introducing 44 stones of 7 cm weighing 5 kg, in a cylinder that rotates around an inclined axis. The cylinder is rotated during 5 hours until 10000 turns. Then the set of dispersed materials are weighed getting "P" in grams. The Deval coefficient is given by the ratio 400/P [55].

- Lifting wave: the front part of the railway track lifts in the direction of movement, the magnitude use to be about the 10% of vertical deflection.

Each train axle passage produces a sleeper stroke to ballast layer (on a freight train 150 strokes can be reached) which, together with the increasing weight of the sleepers (from 300 to 380 kg) may lead to a rapid deterioration of ballast stones. To minimize this deterioration, a maximum value of the coefficient of Los Angeles is required. Particularly, this coefficient should be less than 14%.

So, the main functions of the ballast against the vertical forces are:

- Help to provide stability and damping capacity to the railway track, which reduces the dynamic loads exerted by trains passage.
- Distribute pressures in the platform to avoid reaching the bearing capacity of the ground.
- Withstand particles abrasion that can be consequence of their successive contact with rigid infrastructures such as, for example, concrete bridges.

Table 2.2 summarizes other features required to materials used as ballast. To meet all those functions, the layer thickness should be between 25 and 35 cm [3]. The lower limit is determined by the achievement of objectives, with less ballast the specifications could not be met, while the upper value is set by the need to restrict the seats of the railway track and the geometrical defects.

Abrasion requirements are achieved by requiring the ballast a value over 15 in the Deval coefficient.

Particle shape also affects ballast behaviour, that is why flakiness index and particle length are evaluated. The flakiness index test is performed to determine the number of slabs in the granular material used in the construction of railway tracks. Stretched particles can break, leading to modifications of the particle size and decreasing the expected load capacity. In this context, slabs are the fraction of granular material whose minimum dimension (thickness) is less than 3/5 of the average size of the considered fraction. The test consists of two sifting operations, the first one to separate particles into groups, depending on their size, and the second sift with a parallel bars sieve. The bars of the second sieve are separated 0.5 times the size of the first sieve. The flakiness index is expressed as the weight percentage of ballast passing through the bars sieve. According to the European regulations, this index must be less than or equal to 35%.

The particle length index is defined as, the mass percentage of ballast particles greater than or equal to 100 mm length, in a ballast sample weighting more than 40 kg. The test is performed by measuring each of the particles with a calliper. According to European legislation the particle length index must be lower than 4%.

The most common ballast maintenance operation is mechanical tamping. Its aim is to correct track misalignments by compacting the ballast under the sleepers, providing a solid foundation. If ballast is sufficiently strengthened, then, the stone would occupy the smallest possible volume, increasing the drainage of the platform.

Table 2.2: Ballast properties. Source: CENIT [12].

<table>
<tr><th>Actions</th><th>Functions</th><th>Property</th><th>Property evaluation</th></tr>
<tr><td rowspan="5">Vertical</td><td rowspan="2">Elasticity and damping</td><td>Elastic modulus</td><td>Load plate test</td></tr>
<tr><td>Ballast thickness</td><td>Minimum thickness</td></tr>
<tr><td>Abrasion resistance</td><td>Resistance to abrasion</td><td>Wet MicroDeval</td></tr>
<tr><td>Alleviate pressure on the railway platform</td><td>Ballast thickness</td><td>Minimum thickness</td></tr>
<tr><td>Withstand rail shocks</td><td>Impact resistance</td><td>Los Angeles coeficient</td></tr>
<tr><td rowspan="2">Horizontal</td><td>Longitudinal resistance</td><td rowspan="2">Granulometry</td><td rowspan="2">Granulometric analisys
% fines
Particles maximum length</td></tr>
<tr><td>Transversal resistance</td></tr>
<tr><td rowspan="2">Climate</td><td>Assist the drainage</td><td>Granulometry</td><td>Granulometric analisys
% fines</td></tr>
<tr><td>Ice resistance</td><td>Frost resistance</td><td>Frost resistance
Particle density
Petrography analysis
Water absorption
Resistance to magnesium sulphate</td></tr>
</table>

Sleepers

The elongated pieces made of various materials, located between the rails and the ballast layer are called sleepers, whose main functions are [4]:

- Keep rail position. Sleepers support the two rails maintaining their separation and inclination.
- Distribute vertical, lateral and longitudinal loads from the rails to the ballast.
- Contribute (along with fasteners) to maintain electrical isolation between the two rails, on roads with electrical signals.
- Preserve the horizontal stability of the track, in both directions, lateral and longitudinal, against stresses due to temperature variations or dynamic loads due to the trains passage. Sleepers prevent buckling and ripping (lateral displacement) of rails.
- Preserve the stability of the track in the vertical plane, against static and dynamic loads produced by trains.

The most significant sleeper variables are [4]:

- Dimensions: as the supporting area available is a variable that should be taken into account to reduce the stresses transmitted to the ballast layer.
- Weight: contributes to increase longitudinal and lateral stability of the track.
- Elasticity: along with the fasteners, sleepers provide elastic stability absorbing mechanical forces and preventing deterioration, which minimizes maintenance costs.

Different types of sleepers can be classified according its material or based on their shape. Sleepers, depending on the material, can be classified as wood, steel, cast iron, reinforced concrete, pre-stressed concrete or synthetic sleepers.

According to their shape, sleepers can be monoblock, semi-sleepers or twin block. Figure 2.5 shows a diagram of each of the types.

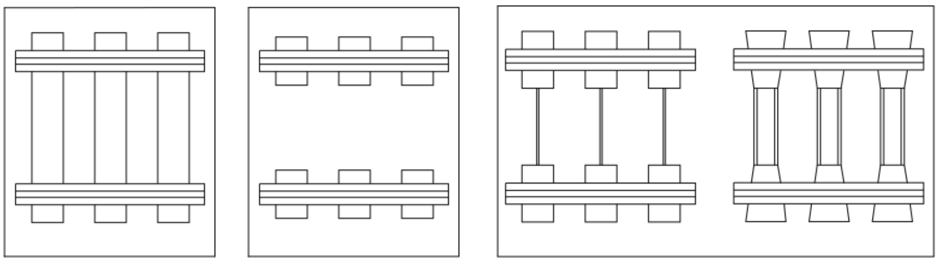

(a) Monoblock. (b) Semi-sleeper. (c) Bi-block.

Figure 2.5: Different types of sleeper depending on the shape. Source: Álvarez and Luque [4].

Although the list of sleeper types may seem large, in Spain, basically three types are used:

- Wood sleepers (Figure 2.6(a)).
- Two different concrete sleepers:
  - Monoblock sleepers (Figure 2.6(b)).
  - Twin block sleepers (Figure 2.6(c)).

(a) Wood sleepers. (b) Monoblock concrete sleepers. (c) Twin block concrete sleepers.

Figure 2.6: Different kind of sleepers, by material and shape.

Wood sleepers, defined in the Standard NRV 3-1-0.0 [40], may be of different kind of trees such as oak, beech or pine. These sleepers must comply the established regulations, which came from 1966 [52].

In the first railway tracks, constructed in the nineteenth century, the only material used to manufacture sleepers was wood, since their physical and mechanical properties, added to its abundance, made this material the best choice. However, time passes and the possibility of using concrete to build sleepers make wood sleepers almost disappear.

Nowadays wood sleepers are used very rarely and never in high-speed lines. Wood sleepers can be used, for example, in tracks where the stiffness of the ballast platform and the structure is very high, like in metal bridges.

Prestressed concrete displaced wood as a material for sleepers manufacturing. These are the most important benefits and drawbacks of concrete sleepers over wood sleepers [3]:

- Advantages of using concrete sleeper instead of wood sleepers:
  - Concrete sleepers have a longer life, about two or three times more than wood sleepers.
  - Their physical conditions are preserved all over the railway track.
  - Better track resistance against displacement in its horizontal plane.
  - Their greater weight provides higher lateral and longitudinal resistance against different forces.
  - Their design can be easily changed to improve track properties.
  - Concrete sleepers cost less than treated wood sleepers.
- Disadvantages of using concrete sleeper instead of wood sleepers:
  - To electrically isolate the two rails, the use of special insulation is needed.
  - Its weight, from 180 to 350 kg, compared to the weight of wood sleepers, 80 kg, make them an element difficult to handle. They are also more brittle.
  - They present a structural weakness at their centre (in case of monoblock sleepers) because their uniform support on ballast produce stresses on their upper face, being able to originate cracks in concrete.

The Standards N.R.V. 3-1-2.1 [41] and N.R.V. 3-1-3.1 [42] describe, respectively, the main features of monoblock and twin block sleepers. In Spain, monoblock sleepers are widely used because of their resistance (monoblock sleepers can be prestressed) and their bigger bearing surface, that allows a better distribution of loads. The advantages of twin block sleepers are that they are lighter and their behaviour to lateral movement is good (in France they are still used frequently). Twin block sleepers main problems are [24]:

- Its high cost due to steel used in its central zone.
- They are not the best sleeper in maintaining rail track width, mainly due to its low vertical and horizontal stiffness.
- Their central strut may be corroded easily.
- Their behaviour against derailment is poor.

Regarding materials used, technical specifications require a high quality cement with high strength and uniform size aggregates and siliceous. The compressive strength of the concrete must be greater than 550 kg/cm^2, and the tensile strength of the steel should be above 150 kg/mm^2.

There are many types of concrete sleepers depending on their dimensions. For monoblock sleepers, which will be the object of study in this work as they are the most used in Spain, technical specification ET 03.360.571.8 [2] establishes the parameters defined in Table 2.3. Those parameters will depend on the type chosen. Figure 2.7 shows some of those parameters.

New sleeper designs should be fully defined in a draft drawing, signed by the applicant, including basic dimensions that the department responsible for the railway infrastructure administration determines. In all cases sleeper length is 2.60 m and the base width in the outer part is equal to 30 cm, excluding very few exceptions.

Table 2.3: Sleeper geometry.

Dimension	Description
L	Concrete element total length
b_i, b_s	Concrete element lower and upper part thickness
h_p	Height in each position along the entire concrete element
L_1	Distance from the outer reference point to the fasteners
L_2	Distance between the outer reference point and the end of the concrete element
I	Tilting of the rail support plane
F	Flatness of each supporting area to two points far away 150 mm
T	Relative torsion between the supporting planes of both rails

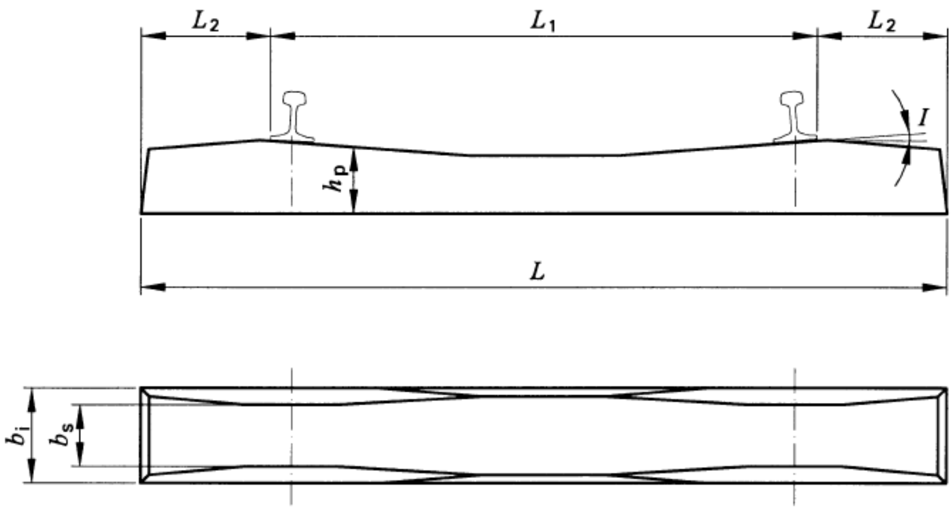

Figure 2.7: Sleeper geometry parameters. Source: Admetlla [3].

Ballast-sleeper friction

Ballast-sleeper friction is one of the most important parameters for the evaluation of railway track load resistance. However, it is a feature very difficult to obtain. Zand and Moraal [62] compared the variation of the lateral force (force needed to move the sleeper laterally) with the variation of vertical load (weight on the sleeper), obtaining a friction coefficient value of 0.7247 (graph of Figure 2.8). They also compared their results with other studies that obtained values between 0.665 and 0.872. This range of values would be the starting point for the calibration of the subsequent simulations.

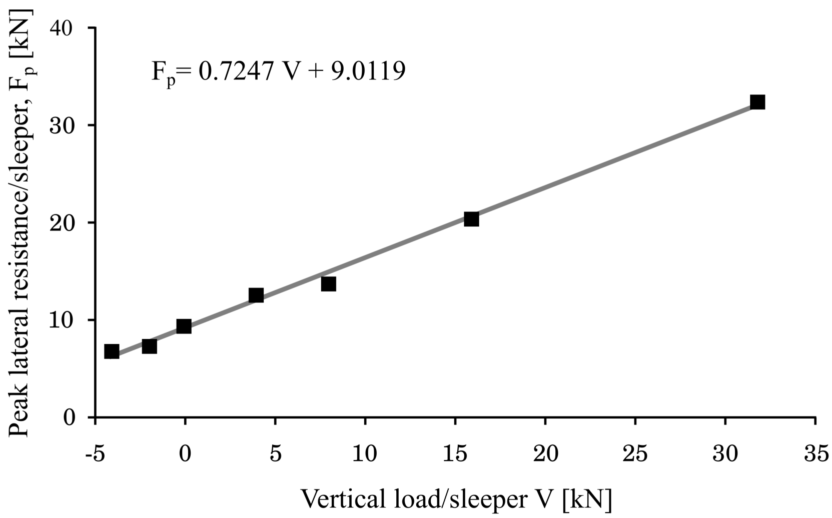

Figure 2.8: Maximum ballast resistance when a lateral displacement is imposed to the sleeper depending on the vertical load. Source: Zand and Moraal [62].

2.2 Discrete Element Method

Since Cundall [14], in 1979, presented the first ideas of the DEM, this numerical technique has increased its popularity being known, nowadays, as a powerful and efficient tool to reproduce the behaviour of granular material.

For the analysis of granular materials with DEM, each grain is represented as a rigid particle. In the first DEM approaches, those particles used to be spheres in 3D and circles in 2D, but now, numerous advances had been developed to represent different geometries. Regardless the geometry of the particles, they interact among themselves in the normal and tangential directions, assuming material deformation concentrated at the contact points.

Material properties are defined by appropriate contact laws that can be seen as the formulation of the material model at the microscopic level.

In the following paragraphs, basic formulation of the DEM will be presented. Special features regrading the development of the DEM for the calculation of ballast material will be treated in chapter 3.

2.2.1 Equations of motion

Basic equations

Standard rigid body dynamics equations define translational and rotational motion of particles. For the i-th particle, movement is calculated as

$$m_i \ddot{\mathbf{u}}_i = \mathbf{F}_i \,, \tag{2.1}$$

$$\mathrm{I}_i \dot{\boldsymbol{\omega}}_i = \mathbf{T}_i \,, \tag{2.2}$$

where $\mathbf{u}_i$ is the particle centroid displacement in a fixed coordinate system $\mathbf{X}$, $\boldsymbol{\omega}_i$ the angular velocity, m_i the particle mass, I_i the moment of inertia second order tensor, $\mathbf{F}_i$ the resultant force, and $\mathbf{T}_i$ the resultant moment about the central axes.

$\mathbf{F}_i$ and $\mathbf{T}_i$ are computed as the sum of: (i) all forces and moments applied to the i-th particle due to external loads, $\mathbf{F}_i^{ext}$ and $\mathbf{T}_i^{ext}$, respectively, (ii) contact interactions with neighbouring spheres $\mathbf{F}^{ij}$, $j = 1, \cdots, n_i^c$, where n_i^c is the number of elements being in contact with the i-th discrete element, (iii) forces and moments resulting from external damping, $\mathbf{F}_i^{damp}$ and $\mathbf{T}_i^{damp}$, respectively, which can be written as

$$\begin{aligned} \mathbf{F}_i &= \mathbf{F}_i^{ext} + \sum_{j=1}^{n_i^c} \mathbf{F}^{ij} + \mathbf{F}_i^{damp} && (2.3) \\ \mathbf{T}_i &= \mathbf{T}_i^{ext} + \sum_{j=1}^{n_i^c} \mathbf{r}_c^{ij} \mathbf{F}^{ij} + \mathbf{T}_i^{damp} && (2.4) \end{aligned}$$

where $\mathbf{r}_{ij}^c$ is the vector connecting the centre of mass of the $i - th$ particle with the contact point c with the j-th particle. Figure 2.9 shows contact forces between spheric particles [48].

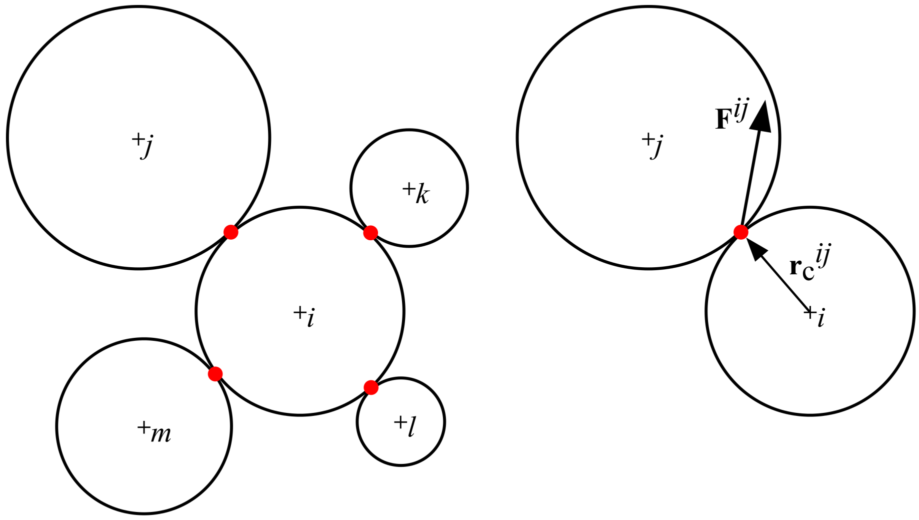

(a) Contact between various particles.

(b) Force between two particles.

Figure 2.9: Force $\mathbf{F}^{ij}$ at the contact interface between particles i and j. Source: Oñate and Rojek [48]

Integration of equations of motion

Equations (2.1) and (2.2) are integrated in time using a simple forward Euler scheme. The translational motion at the n-th time step is calculated as follows:

$$\ddot{\mathbf{u}}_i^n = \frac{\mathbf{F}_i^n}{m_i}\,, \tag{2.5}$$

$$\dot{\mathbf{u}}_i^n = \dot{\mathbf{u}}_i^{n-1} + \ddot{\mathbf{u}}_i^n \Delta t \tag{2.6}$$

$$\mathbf{u}_i^{n+1} = \mathbf{u}_i^n + \dot{\mathbf{u}}_i^n \Delta t \tag{2.7}$$

The integration scheme for the rotational motion is:

$$\dot{\boldsymbol{\omega}}_i^n = \frac{\mathbf{T}_i^n}{\mathbf{I}_i}\,, \tag{2.8}$$

$$\boldsymbol{\omega}_i^n = \boldsymbol{\omega}_i^{n-1} + \dot{\boldsymbol{\omega}}_i^n \Delta t \tag{2.9}$$

$$\Delta\boldsymbol{\theta}_i = \boldsymbol{\omega}_i^n \Delta t \tag{2.10}$$

Explicit integration in time yields high computational efficiency and enables the solution of large models. The disadvantage of the explicit integration scheme is its conditional numerical stability, imposing the limitation on the time step Δt [64]. The critical time step is determined by the highest natural frequency of the system.

2.2.2 Frictional contact conditions

Contact search algorithm

The search for new particle contacts is the most time-consuming operation in the DEM calculation. The simplest approach to identify interaction pairs, by checking every sphere against every other sphere would be very inefficient, as the computational time is proportional to n^2, where n is the number of elements. For that reason, some search algorithms based on quad-tree and oct-tree structures have been developed. Those formulations allow reduction of the necessary time to become proportional to $(n \cdot \ln n)$, which allows to solve large frictional contact systems [31].

Decomposition of the contact force

Once contact between a pair of elements has been detected, the forces occurring at the contact point are calculated. The contact between the two interacting spheres can be represented by the contact forces $\mathbf{F}^{ij}$ and $\mathbf{F}^{ji}$ (Figure 2.9), which satisfy the following relation:

$$\mathbf{F}^{ij} = -\mathbf{F}^{ji} \tag{2.11}$$

$\mathbf{F}^{ij}$ is decompsed into the normal and tangential components, $\mathbf{F}_n^{ij}$ and $\mathbf{F}_s^{ij}$, respectively (Figure 2.10)

$$\mathbf{F}^{ij} = \mathbf{F}_n^{ij} + \mathbf{F}_t^{ij} = F_n \mathbf{n}^{ij} + \mathbf{F}_t^{ij} \tag{2.12}$$

where $\mathbf{n}^{ij}$ is the unit vector normal to the particle surface at the contact point between particles i and j. This implies that it lies along the line connecting the centres of the two particles. Its direction is outwards from particle i.

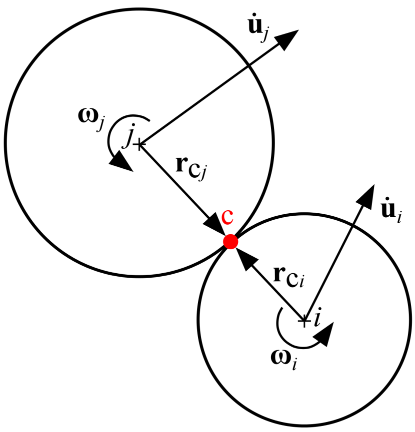

(a) Contact between two particles.

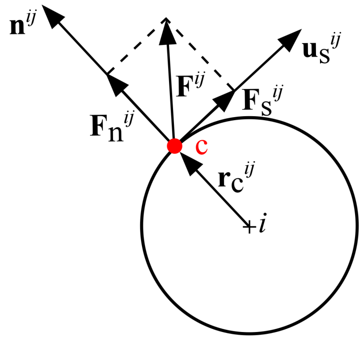

(b) Contact force decomposition.

Figure 2.10: Decomposition of the contact force into normal and tangential components. Source: Oñate and Rojek [48].

The tangential force $\mathbf{F}_t^{ij}$, along the tangential direction $\mathbf{u}_t^{ij}$ (Figure 2.10), can be written as

$$\mathbf{F}_t^{ij} = F_{t_1} \dot{\mathbf{u}}_{t_1} + F_{t_2} \dot{\mathbf{u}}_{t_2} \tag{2.13}$$

where F_{t_1} and F_{t_2} are the tangential force components along the tangential direction $\dot{\mathbf{u}}_{t_1}$ and $\dot{\mathbf{u}}_{t_2}$, respectively.

The tangential force modulus F_t is obtained by

$$F_t^{ij} = |\mathbf{F}_t^{ij}| = (F_{t_1}^2 + F_{t_2}^2)^{1/2} \tag{2.14}$$

The contact forces F_n, F_{t_1} and F_{t_2} are obtained using a constitutive model formulated for the contact between two rigid particles. Typical DEM local constitutive models are described in the following section.

2.2.3 DEM constitutive models

Standard constitutive models in the DEM are characterized by the parameters shown in Figure 2.11.

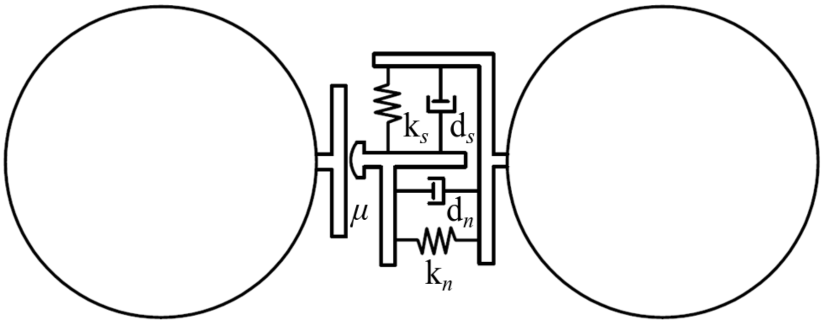

Figure 2.11: DEM standard contact interface. Source: Oñate et al. [49].

Those parameters are:

- Normal and tangential stiffness parameters k_n and k_t.
- Normal and tangential local damping coefficients d_n and d_t at the contact interface.
- Coulomb friction coefficient μ.

Normal contact force

In the basic DEM, the normal contact force F_n is decomposed into the elastic part F_{ne} and the damping contact force F_{nd}:

$$F_n = F_{ne} + F_{nd} \tag{2.15}$$

In general, the normal elastic interaction force can be described as follows:

$$F_{ne}^c = k_n \delta^\alpha \tag{2.16}$$

where F_{ne}^c is the normal elastic force in the contact point (c), k_n the normal stiffness parameter, δ the indentation (penetration between both particles that is shown in Figure 2.12) and α is a parameter that depends on the constitutive model.

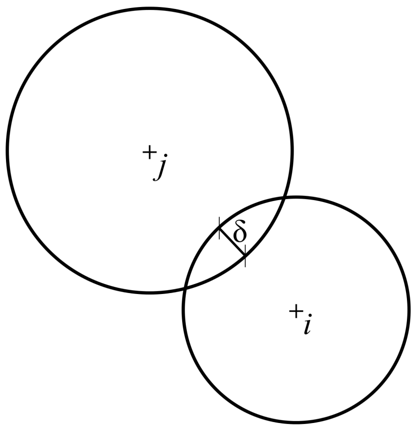

Figure 2.12: Indentation between two particles in contact.

The most common constitutive models, for the calculation of granular material normal contact force with DEM are: linear and Hertz models.

Considering contact between spheres with Young modulus equal to E_i and E_j, Poisson ratio equal to ν_i and ν_j and radius equal to r_i and r_j respectively, the normal force parameters for the linear constitutive model are:

$$k_n = \frac{2\pi E_1 E_2 (r_i r_j)^2}{(E_1 + E_2)(r_i + r_j)^3} \quad , \quad \alpha = 1 \tag{2.17}$$

The Hertz contact model is an approach that takes into account the curvature of the contacting surfaces. When one body touches another one, the contact point is deformed, but that contact area is very small compared with the dimensions of the contacting bodies. The shape of the contact area, its increase and the stress distribution along that region is acquired from the geometry of the contacting bodies and the load applied [28].

It should be noted that, the Hertz contact model can only be applied in static cases or when the impact velocity is small. The impact velocity limit depends on the density and Young modulus of the material, Johnson [28] set a criterion to know which is the maximum impact velocity for applying the Hertz contact model.

In case of two spheres with radius r_i and r_j the contact area is a circle of radius a, as shown in Figure 2.13.

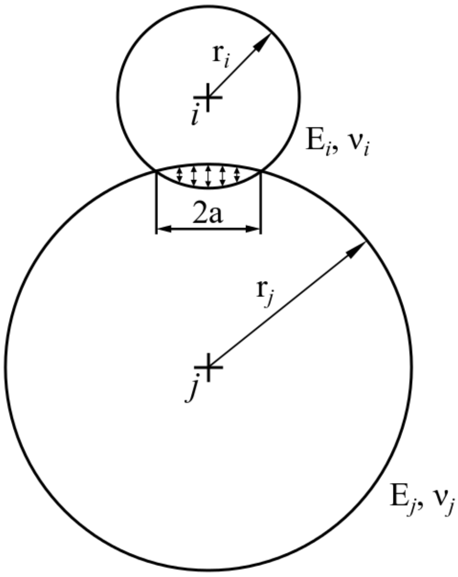

Figure 2.13: Hertz contact model scheme.

From those relations, the normal force stiffness parameters k_n for the Hertz constitutive model can be derived:

$$k_n = \frac{4}{3}\frac{E_i E_j}{E_j(1-\nu_i^2)+E_i(1-\nu_j^2)}\sqrt{\frac{r_i r_j}{r_i + r_j}} \quad , \quad \alpha = 1.5 \tag{2.18}$$

Damping contact force is calculated in the same way for linear and Hertz contact constitutive models:

$$F_{nd}^c = d_n \cdot \Delta v_{rn} \tag{2.19}$$

where v_{rn} is the normal relative velocity of the centres of the two particles in contact:

$$v_{rn} = (\dot{\mathbf{u}}_j - \dot{\mathbf{u}}_i) \cdot \mathbf{n}^{ij} \tag{2.20}$$

and d$_n$ depends on the *restitutions coefficient* c$_r$, that represents the percentage of energy the system returns after a collision.

$$d_n = -(\ln c_{ri} + \ln c_{rj})\sqrt{\frac{\frac{m_i m_j}{m_i+m_j}k_n}{(\frac{\ln c_{ri}+\ln c_{rj}}{2})^2+\pi^2}} \tag{2.21}$$

Tangential frictional contact

Tangential force $\mathbf{F}_t$ appears by friction opposing the relative motion at the contact point. The relative tangential velocity at the contact point $\mathbf{v}_{rt}$ is calculated from the following relationship:

$$\mathbf{v}_{rt} = \mathbf{v}_r - (\mathbf{v}_r \Delta \mathbf{n})\mathbf{n} \tag{2.22}$$

with

$$\mathbf{v}_r = (\dot{\mathbf{u}}_j + \omega_j \times \mathbf{r}_{cj}) - (\dot{\mathbf{u}}_i + \omega_i \times \mathbf{r}_{ci}) \tag{2.23}$$

where $\dot{\mathbf{u}}_i$, $\dot{\mathbf{u}}_j$ and ω_i, ω_j are, respectively, the translational and rotational velocities of the particles, and $\mathbf{r}_{ci}$ and $\mathbf{r}_{cj}$ are the vectors connecting particle centres with contact points.

The relationship between the friction force $||\mathbf{F}_t||$ and the relative tangential displacement $\mathbf{u}_{rt}$, for the classical Coulomb model (for a constant normal force $\mathbf{F}_n$) is shown in Figure 2.14(a). This relationship would produce non physical oscillations of the friction force in the numerical solution, due to possible changes of the direction of sliding velocity. To prevent this, the Coulomb friction model must be regularized. The regularization can be seen in Figure 2.14(b)

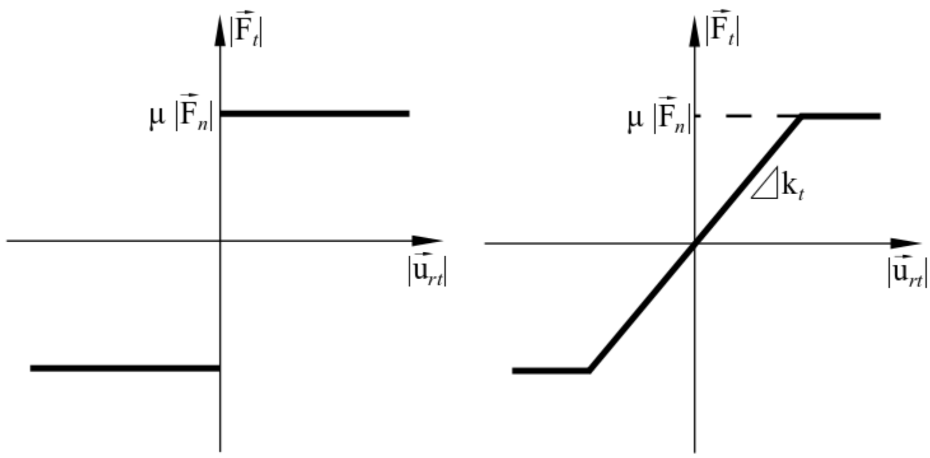

(a) Classical Coulomb law. (b) Regularized Coulomb law.

Figure 2.14: Friction force vs. relative tangential displacement graph for classical and regularized Coulomb law. Source: Santasusana [54].

This is equivalent to formulating the frictional contact as a problem analogous to that of elastoplasticity, which can be seen clearly from the friction force-tangential displacement relationship in Figure 2.14(b).

To perform this calculation an standard radial return algorithm is used, as follows:

$$\mathbf{F}_t^{trial} = \mathbf{F}_t^{old} - k_t \mathbf{v}_{rt} \Delta t, \tag{2.24}$$

and then the slip condition is checked:

$$\phi^{trial} = ||\mathbf{F}_t^{trial}|| - \mu |\mathbf{F}_n|. \tag{2.25}$$

If $\phi_{trial} \leq 0$ there is not slip in the contact and the friction force is equal to the trial value:

$$\mathbf{F}_t^{new} = \mathbf{F}_t^{trial}, \tag{2.26}$$

otherwise (slipping contact), force is calculated as follows:

$$\mathbf{F}_t^{new} = \mu|\mathbf{F}_n|\frac{\mathbf{F}_t^{trial}}{||\mathbf{F}_t^{trial}||}, \tag{2.27}$$

Tangential damping can be also applied:

$$F_{td}^c = d_t \cdot \Delta v_{rt} \tag{2.28}$$

In that case, the tangential damping coefficient is:

$$d_t = d_n\sqrt{\frac{k_t}{k_n}} \tag{2.29}$$

2.2.4 Discrete-Finite elements interaction

In section 2.2.2 contact search algorithm has been mentioned. Now, not only discrete element search has to be performed, but also finite element search. The basic idea is summarized in the following paragraphs.

Global search algorithm

In a generic way, there are two types of elements: searcher elements (particles) and target elements (particles or finite elements). Hereafter searcher elements will be called S.E. and target elements T.E.

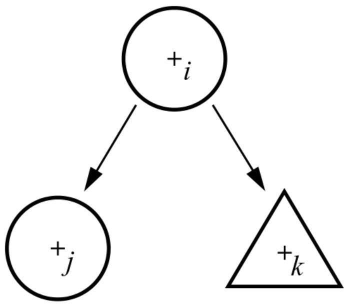

Figure 2.15: Two types of search needed. Element i is the S.E. and elements j and k are the T.E.

The steps needed to perform contact search are:

a) Build bounding box of S.E. (Figure 2.16(a)).

b) Build bins cells based on size and position of S.E. (Figure 2.16(b)).

c) Collocate S.E. in bins and construct hash table with relates coordinates with cells which point to the contacting S.E. (Figure 2.16(c)).

d) Build bounding box of T.E. (Figure 2.16(d)).

e) Loop over T.E., detect the intersecting cells to each T.E., check the intersection with the possible found cells and add the entire S.E. contained in the cells intersected by each T.E. (Figure 2.16(e)).

f) Solve the contact with local resolution (Figure 2.16(f)).

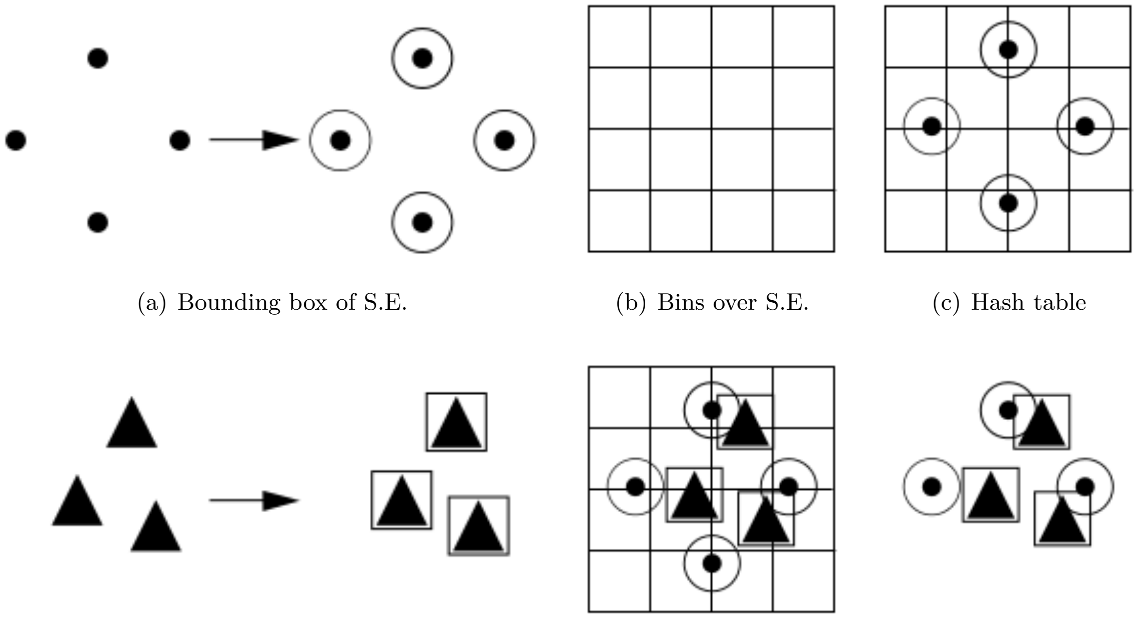

(a) Bounding box of S.E. (b) Bins over S.E. (c) Hash table

(d) Bounding box of T.E. (e) Intersection cells. (f) Local resolution.

Figure 2.16: Sketch showing the search algorithm. Source: Santasusana [54].

Local search resolution

Once the possible neighbours are detected, the local resolution check takes place. For the case of two spherical particles, the check is easy; only the sum of the radius has to be compared against the distance between centres. Other geometries may demand a much complicated check.

The followed strategy is to mesh all the geometries with a discretization of triangles. In 3D, surface meshes are used for contact detection. Now, the contact detection should be performed between particles and triangles; if no contact is found, particle contact against lines is searched for; and if contact is still not found, contact against points is performed. Figure 2.17 shows how the local search is performed. Particle i searches contact against element j, then against lines k, l and m and finally against points n, o and p.

This algorithm has some drawbacks and it does not work properly in all situations. The solution adopted to those problems in this work will be presented in section 3.2.3.

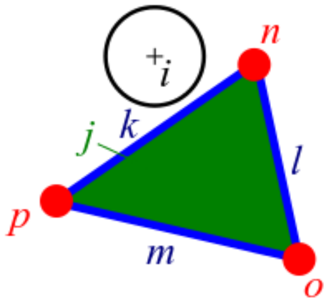

Figure 2.17: Particle-Face contact detection.

Changes in the Finite Element Method

After contact detection, force applied from particles to finite elements is calculated and transferred to the nodes via a weighting algorithm. To adequately couple both methods, a finite element explicit solution strategy is the best choice, as a explicit strategy is being used for discrete element calculation. For the finite elements solution, Rayleigh damping is commonly used [54].

3 NUMERICAL MODEL

This chapter presents the code implementations developed in this work. Those implementations were performed due to the limitations of the previous code for the simulation of ballast material laboratory tests.

3.1 Kratos and DEM-application

The code has been implemented inside *Kratos*, an Open-Source framework for the implementation of numerical methods for the solution of engineering problems. All above commented in section 2.2 has already been implemented in the so called *DEM-application*. In this chapter, contributions to the code from this work will be presented. The whole program is called *DEMpack*.

Figure 3.1: Computer programs used and improved.

3.2 Contributions to the code

The computational cost of contact calculation between irregular particles with DEM is high and limits the simulation capability. For that reason, ballast characterization has initially been carried out using spherical discrete elements. The local constitutive law of classical DEM has been modified by introducing an additional particle parameter called rolling friction coefficient [31].

When a big amount of granular material is involved in the calculation, the geometric simplification due to the use of spheres has been considered acceptable. In case of a micro-scale analysis or calculations with a small amount of grains, this kind of simplifications would not be appropriate. For that reason, it is also possible to perform calculations using sphere clusters, a bunch of superposed spheres that represent the particle geometry. Sphere clusters build up and calculation will be explained in section 3.2.2.

3.2.1 Rolling friction

Rolling friction approach consist in imposing a virtual moment opposite to particle rotation and dependent on its size. Figure 3.2 shows schematically how does rolling friction in two dimensions work.

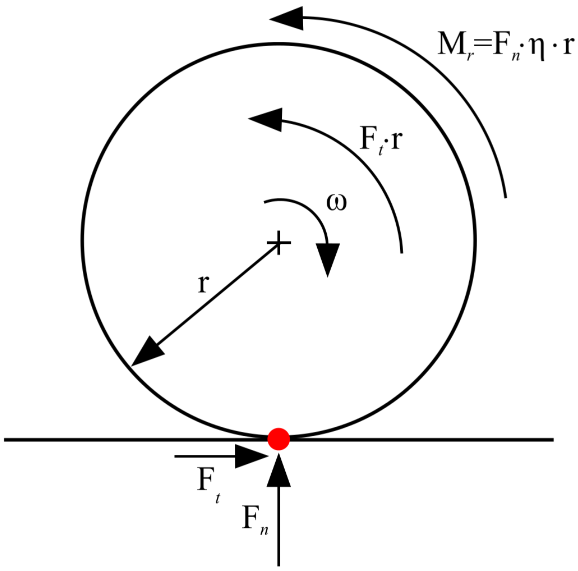

Figure 3.2: Two dimension simplified scheme of rolling friction.

F_n represents the normal force, F_t the tangential force, ω the angular velocity, r is the radius and η the rolling friction coefficient.

The rolling friction coefficient is a material parameter that depends on the shape of the particles. A granular material composed of sharp stones will have a larger rolling friction coefficient than a material composed of spherical and soft stones.

The implementation of the rolling friction has been developed as follows:

1. The initial maximum resisting moment (M^{ini}_{max}) is the moment, opposite to the sphere rotation, needed to stop the sphere rotation in one time step. This has to be calculated to prevent the rolling friction change the direction of the particle spin.

Equations 3.1 and 3.2 show the calculation of M_{max}^{ini} where: ω is the current initial angular velocity of the sphere, $\dot{\omega}_{stop}$ is the angular acceleration needed to completely stop the sphere rotation in one computational time step (Δt) and I is the particle moment of inertia.

$$\dot{\omega}_{stop} = -\omega \cdot \Delta \mathrm{t} \tag{3.1}$$

$$\mathrm{M}_{max}^{ini} = \dot{\omega}_{stop} \cdot \mathrm{I} \tag{3.2}$$

2. Forces and moments due to contact are calculated. After force computation, moment will be equal to tangential force multiplied by particle radius. Now, the maximum resisting moment is calculated (M_{max}) being the initial maximum resisting moment (M_{max}^{ini}), already computed, minus the contact moment.

$$\mathrm{M}_{max} = \mathrm{M}_{max}^{ini} - \mathrm{F}_t \cdot \mathrm{r} \tag{3.3}$$

3. The computation of the maximum theoretical moment (M_{theor}) is carried out from the normal force and the rolling friction coefficient.

$$\mathrm{M}_{theor} = \eta \cdot \mathrm{r} \cdot \mathrm{F}_n \tag{3.4}$$

4. The maximum resisting moment (M_{max}) and the maximum theoretical moment (M_{theor}) are compared, so the resisting moment (M_r) can be computed. Equations 3.5 and 3.6 show the procedure.

$$\text{if } \|\mathrm{M}_{theor}\| \geq \|\mathrm{M}_{max}\| \rightarrow \mathrm{M}_r = \mathrm{M}_{max} \tag{3.5}$$

$$\text{if } \|\mathrm{M}_{theor}\| < \|\mathrm{M}_{max}\| \rightarrow \mathrm{M}_r = \mathrm{M}_{theor} \tag{3.6}$$

5. If there are more contacts with other particles the procedure will be the same for each one.

The sketch in Figure 3.2 and the rolling friction procedure description were presented as a two-dimensional approach, due to the fact that, in two dimensions only exist one rotational direction, that will ease the explanation because the absolute value of the variables and scalar products can be used. In three dimensions the calculation is very similar, the only extra condition that should be taken into account is that the rolling friction moment direction is always against particle rotation.

3.2.2 Sphere clusters

Although, at its simplest, particles within a DEM model may be represented by spheres, the use of non-spherical elements is recognised as essential to give a better approximation to the irregular shape of real particles. Implementations using 3D polyhedra [45], [46], [33], [32] or continuous superquadric functions [50], [13] among others [18] have been reported. While these techniques allow a good representation of real objects, complex algorithms are required to detect and resolve contacts between particles [29]. This leads to deterioration in simulation speed as particle complexity increases.

An alternative approach is to implement techniques that consider particles as clusters of spheres, thereby allowing the use of algorithms that are straightforward extensions of the efficient methods used for spheres [47]. This approach has been used to simulate rigid clusters of spheres in tetrahedral and cubic arrangements [60], axisymmetric particles and tablet-shaped particles [57].

The use of sphere clusters for representing ballast stones [34], [39] or other kind of particles [21] has also been addressed. These approaches incorporate spheres overlap, which allows the algorithm to generate realistic particles using relatively modest numbers of spheres, which is an advantage in terms of computational cost.

In this work a similar overlapping approach is used. The *Sphere-Tree Construction Toolkit* (STCT) employed (`http://isg.cs.tcd.ie/spheretree/`) has implemented a number of algorithms for the construction of sphere-trees [9], [8], [10].

The steps to generate sphere clusters, adapted to a given geometry, using the STCT to be employed in *Kratos DEM-application* are:

1. The starting point should always be the geometry of the particle. In this work *GiD*[5], is being used. Particle geometry can be generated by the user or obtained by scanning real particles.

2. A triangular surface mesh should be generated from the outer surface of the particle (Figure 3.3).

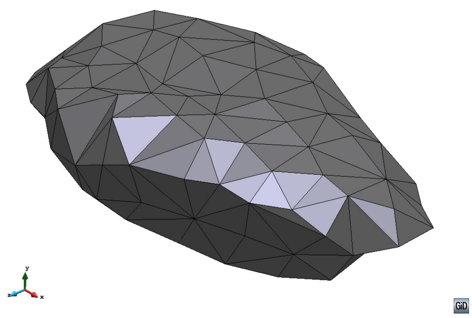

Figure 3.3: Triangular surface mesh of a user defined particle.

3. The triangular surface mesh has to be exported as OBJ format, which is the input format of the STCT. OBJ file format is a simple data format that represents 3D geometry

[5]GiD is a universal, adaptive and user-friendly pre and postprocessor for numerical simulations in science and engineering. It has been designed to cover all the common needs in the numerical simulations field from pre to post-processing: geometrical modeling, effective definition of analysis data, meshing, data transfer to analysis software, as well as the visualization of numerical results. GiD is developed in CIMNE

including only the position of each vertex, the position of each vertex UV[6] and the normal vector to each polygon that composes the outer surface of the volume.

4. After opening the OBJ file with STCT (Figure 3.4) the sphere mesh can be generated. In this work the optimised reduced Hubbard method has been used [9], [25].

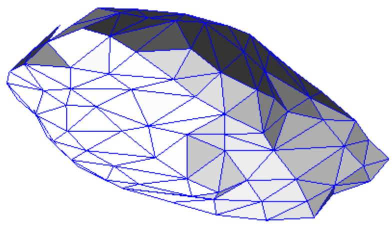

Figure 3.4: OBJ format mesh visualized with STCT.

5. The sphere cluster model is saved in SPH format, characteristic format of the STCT:

   - The number of clusters included in the file and the number of spheres of the biggest cluster is displayed in the first line. In the example shown in Figure 3.5 the same particle is represented as a cluster of 5 (Figure 3.5(a)) and 34 (Figure 3.5(b)) spheres respectively.

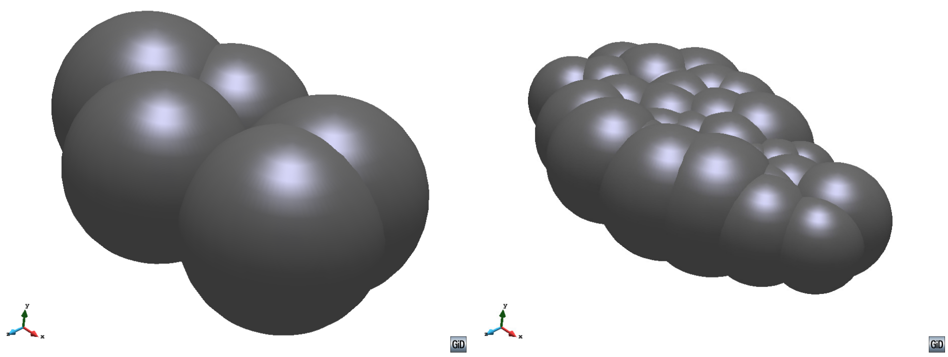

(a) 5 spheres cluster. (b) 34 spheres cluster.

Figure 3.5: Same particle cluster generated with 5 and 34 spheres.

   - The second line of the SPH file presents the central coordinates and the radius of a cluster composed only of one sphere.
   - The following lines contain the coordinates of the centres of the spheres and their radius for clusters with more than one sphere.

6. At this point clusters are already generated. Now the next step is to calculate the geometric features to create the *Kratos* element correctly. To do this:

   - All the spheres should be drawn in a CAD program, in this case *GiD*, and collapsed in order to obtain one single volume. This volume has to be meshed with

[6]Vertex used in UV mapping, which is the 3D modeling process of making a 2D image representation of a 3D model's surface

tetrahedra. The finer the mesh is, the best the properties of the cluster should be defined.

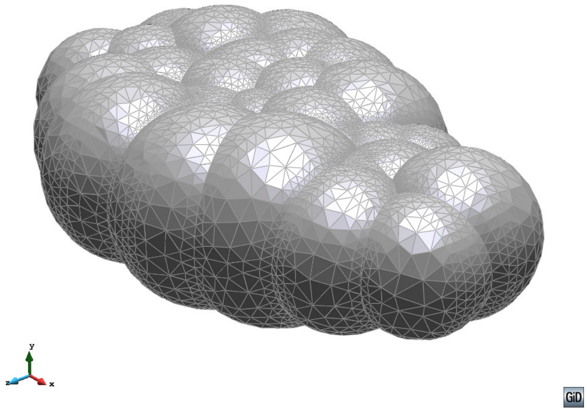

Figure 3.6: Tetrahedra mesh of a spheres cluster.

- The generated tetrahedra mesh is used to calculate the inertia tensor, the centre of mass and the volume of the cluster. Those properties are obtained by means of one of the utilities within the *Kratos Solid Mechanics-application* (available in "rigid body utilities").

7. Cluster elements in the *DEM-application* should be defined by the position of the spheres and their radius, provided that the centre of mass is located at the origin of coordinates. Moreover, the inertia tensor of the particle should be diagonalized. If those conditions are not already met (general case if the clusters are generated using the STCT), appropriate transformations (translations and rotations) must be performed.

In this work, four different sphere clusters representing ballast stones were created. As it was impossible to find data of real ballast geometries, the stones were user-defined according to the regulations defined in section 2.1.5. A sphere cluster calculation will be described in section 4.2.

3.2.3 DE-FE contact improvements

This section summarizes the code improvements developed in the *DEM-application* related to DE-FE contact detection. In the first part those improvements will be described, while in the second part the validation of the method for rigid finite elements calculation will be presented. For elastic finite elements there are some limitations that are already being studied. Anyhow, the method can be successfully applied for contact between discrete and elastic finite elements in quasi-static calculations (for example, the triaxial test presented in section 4.2).

Improved detection of contact between discrete and finite elements

The following figures show two-dimensional schematic graphics of some of the problematic cases when dealing with discrete-finite element detection. The code implementation has been made for three dimensions, but it is equivalent in two dimensions and the procedure can be more clearly seen.

When the finite element mesh used is smaller than the contact area (small finite elements and soft discrete material), something similar to Figure 3.7 could happen.

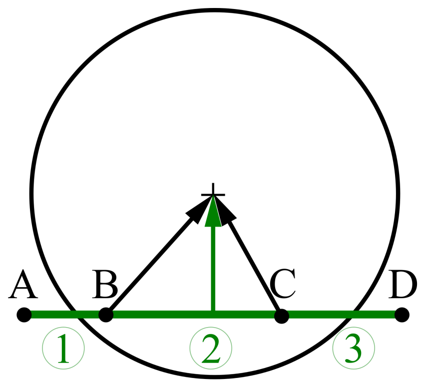

Figure 3.7: Contact between a discrete element and a finite element mesh with a mesh size smaller than the indentation.

As explained in section 2.2.4 neighbour search is always done from the point of view of the sphere. In other words, it is the spherical discrete element which seeks the elements in contact to it. To do this, the distances from the centre of the sphere in Figure 3.7 to items 1, 2 and 3 are measured. If a normal vector to the surface of these elements passes through the centre of the sphere (element 2), contact between the sphere and the plane element exists and it is saved. If there is not any normal vector to the surface of any other element that passes through the centre of the sphere, contact search continues, looking for contact with adjacent axes or points forming those elements (in this case, elements 1 and 3).

Contact point between an sphere and an axis is the nearest point to the centre of the sphere that belongs to the axis (contact only exists if the distance between both is smaller than the sphere radius). The normal contact force vector direction is the same as the direction of the line that joins the centre of the spheric particle and the contact point belonging to the line.

Contact between a point and a sphere is easy to determine, because it only exists if the distance between the point and the centre of the sphere is less than the sphere radius. The normal contact force vector direction is the direction of a line joining the centre of the sphere and the point.

Once all surfaces, axes and points contacts are found, the force that each one exerts to the discrete element should be calculated. However, in the case of Figure 3.7, an important change has to be made first. The force applied by the surface to the sphere must have the direction of the normal vector to the plane, that is, the force applied by axes B and C, should not be taken into account, since the elements 1, 2 and 3 are coplanar. To do this, before calculating the force, all contact vectors are projected over each other to eliminate those that should not be taken into account.

Figure 3.8 graphically shows how to make this contact projection. Analytically, the projection is performed by the dot product of two contact vectors (vectors that join each contact point with the centre of the sphere). Once calculated the dot product of contact vectors, the length of contact vectors and projections is compared, discarding all those cases in which the projection is greater than or equal any other contact vector. For example, in the case of Figure 3.8 no contacts with axes B and C are taken into account, since their projections over the contact vector with surface 2 has the same module as the contact vector itself.

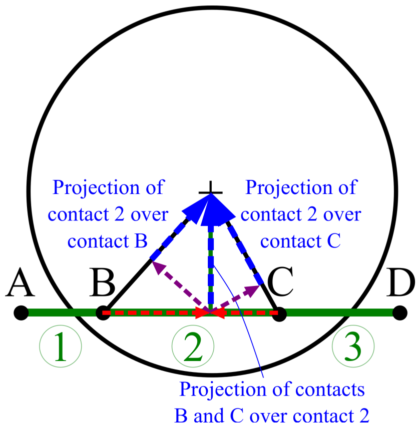

Figure 3.8: Length comparison of contact vectors and their respective projections.

The following chart summarizes the contact check algorithm when the discrete element is in contact with n finite elements. Contact vectors are called $\mathbf{v}_i$ and $\mathbf{v}_j$ and projection vectors $\mathbf{pr}_{i,j}$.

Loop over contact vectors (for i=1,...,n)

Loop over contact vectors (for j=1,...,n)

Perform contact check comparing only with other contact vectors (if i $\neq$ j)

Perform dot product of contact vectors: $\mathbf{pr}_{i,j} = \mathbf{v}_i \cdot \mathbf{v}_j$

Discard invalid contacts: if $\mathbf{pr}_{i,j} \geq \mathbf{v}_j \Rightarrow$ no contact (loop break)

If there is not any contact that fulfils $\mathbf{pr}_{i,j} \geq \mathbf{v}_j$, $\mathbf{v}_i$ should be saved as a valid contact vector

The advantage of this method lies in its generality. The tests carried out show that the force vector always has the appropriate direction. A simple example can be seen in Figure 3.9. In this case, the sphere is in contact with surface 1 and axis C, and both contacts must be taken into account. As shown in Figure 3.9 the projection of each contact vector over the other is smaller than the vectors themselves, so that none of them is discarded.

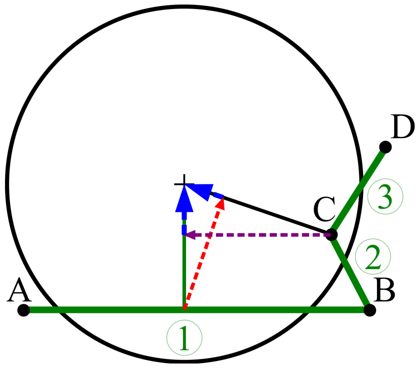

Figure 3.9: Example of more than one valid contact.

Contact detection method validation

Some benchmarks have been carried out for testing the method, obtaining satisfactory results. These simulations are very extreme and do not represent reality; they merely serve to validate the code.

- **Contact between sphere and plane:** This is the simplest case. The performed calculation is a sphere, whose stiffness is very low, contacting with a surface meshed of triangles. In Figure 3.10 the sphere can be seen before contacting the surface.

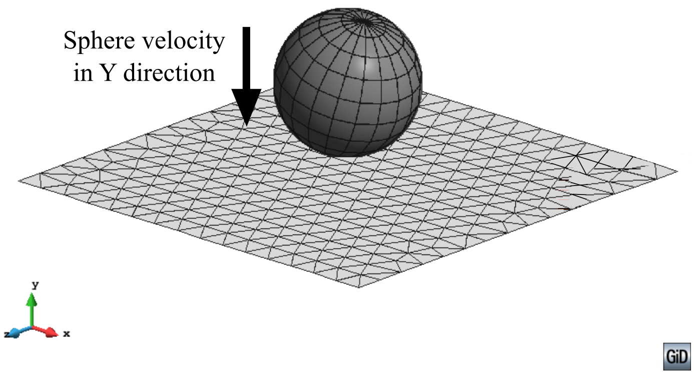

Figure 3.10: Instant before the sphere contacts the surface.

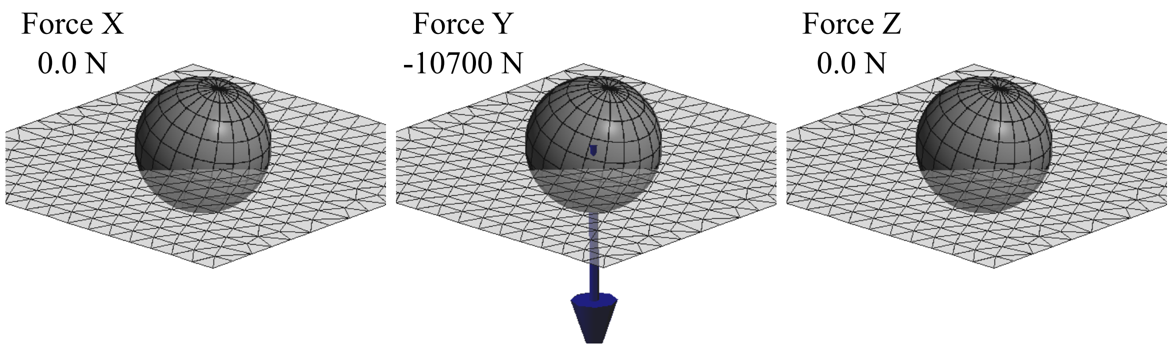

(a) Force in X direction. (b) Force in Y direction. (c) Force in Z direction.

Figure 3.11: Force exerted by the sphere on the plane at the moment of maximum indentation.

Figure 3.11 shows the force applied by the sphere on the plane. The force is applied in the Y axis direction, normal to the plane, so it can be concluded that the method works correctly in this case.

- **Contact between sphere and axis:** This test is similar to the previous one, but now the sphere contacts the axis of two wedge-shaped planes. The simulation in a pre-contact instant is shown in Figure 3.12.

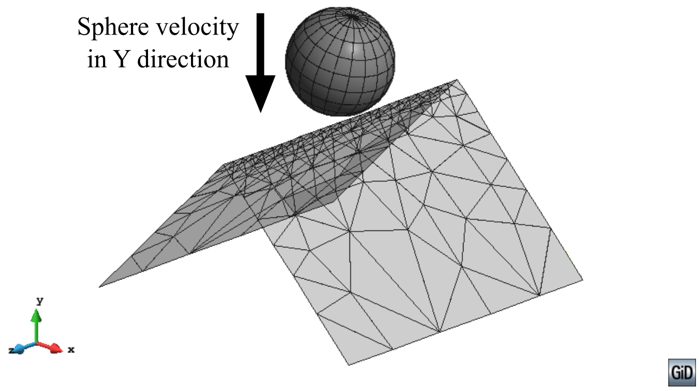

Figure 3.12: Instant before the sphere contacts the axis.

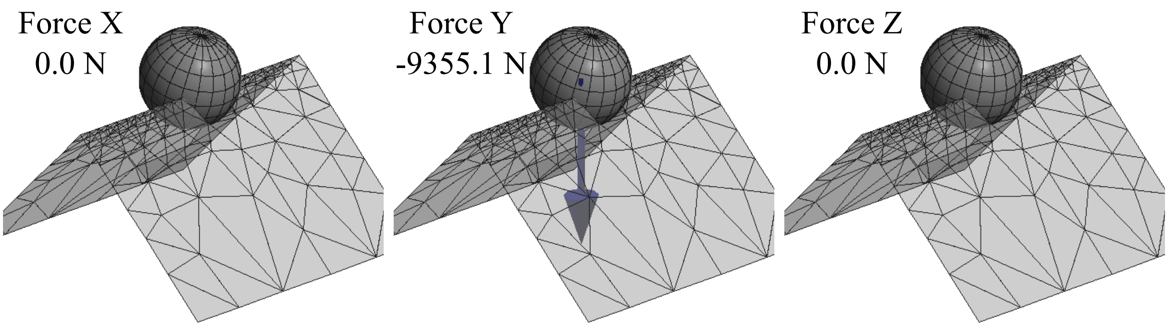

(a) Force in X direction. (b) Force in Y direction. (c) Force in Z direction.

Figure 3.13: Force exerted by the sphere on the axis at the moment of maximum indentation.

As in the previous test, the results are correct. Force is only applied in Y axis direction.

- **Contact between sphere and point:** In this example, a kind "pyramid" has been used to check if the method works correctly for sphere-point contact. The sphere falls upon the top of the "pyramid" as it can be seen in Figure 3.14. In this case the direction of the force must also be applied on the Y axis, as in the previous examples. Figure 3.15 shows that the calculation is accurate.

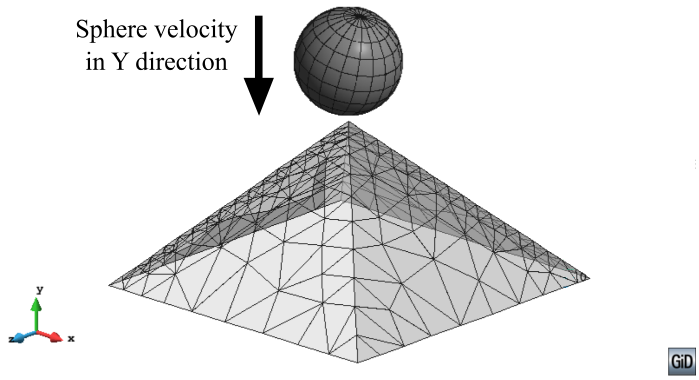

Figure 3.14: Instant before the sphere contacts the corner point.

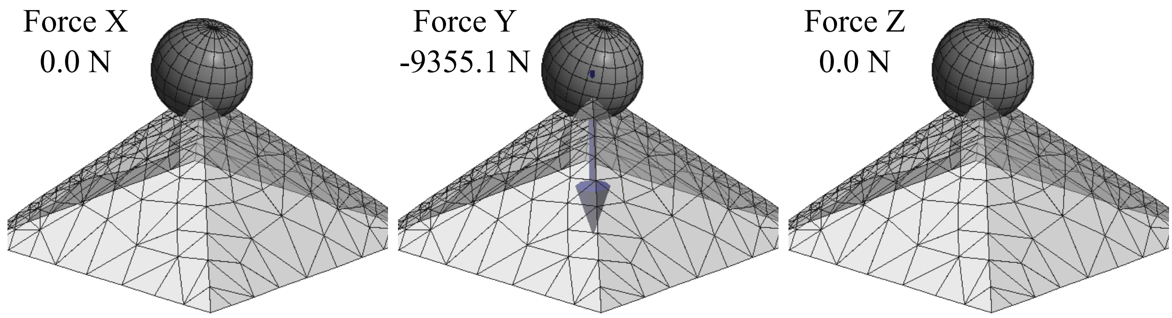

(a) Force in X direction.

(b) Force in Y direction.

(c) Force in Z direction.

Figure 3.15: Force exerted by the sphere on the corner point at the moment of maximum indentation.

It is found that, for all the previous three examples, the force is applied only in the Y axis direction. Therefore, it can be concluded that the method works properly for all three types of possible contact: with surface (plane), with line (axis) and point (corner).

After verifying that the contact detection method works properly for single contacts, some other tests have been developed to validate it under different geometric arrangements.

- **Multiple contact:** The simulation presented below is used to check if the contact between a sphere and more than one element is calculated properly. To do this, three spheres fall upon a plane with three different shape holes, as shown in Figure 3.16.

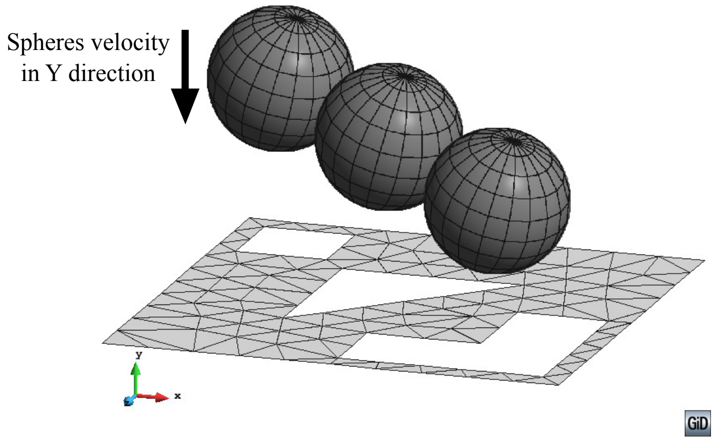

Figure 3.16: Instant before contact.

In Figure 3.17 the position of the spheres at the end of the simulation can be seen when they are at rest. Spheres velocity after 2.5 seconds of simulation is close to 0, as expected.

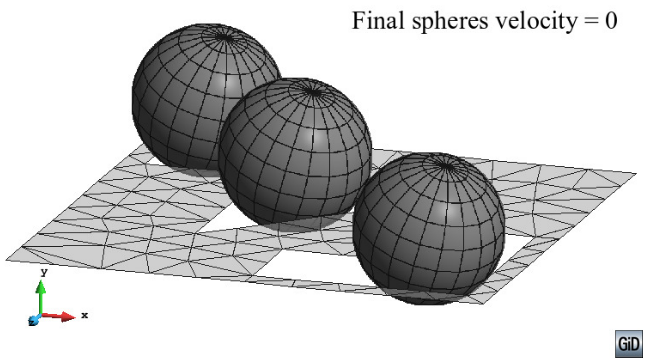

Figure 3.17: Motionless spheres after 2.5 seconds of simulation.

- **Continuity of contact:** Continuity of force magnitude when a discrete element goes from being in contact with the surface of a triangular element to be in contact with one of its axes or points is essential. In his doctoral thesis Wellmann [61] proposes a method to correct force direction and ensure its continuity, based on the area of the intersection of the sphere with the surface.

  The method presented in this work should not need any adjustment to ensure force magnitude continuity and force direction correctness. To check this, a ball without rotation and without friction is moved over a step (as shown in Figure 3.18), setting the path of its centre, so that the indentation is always the same (either in contact with the surface or with the axis).

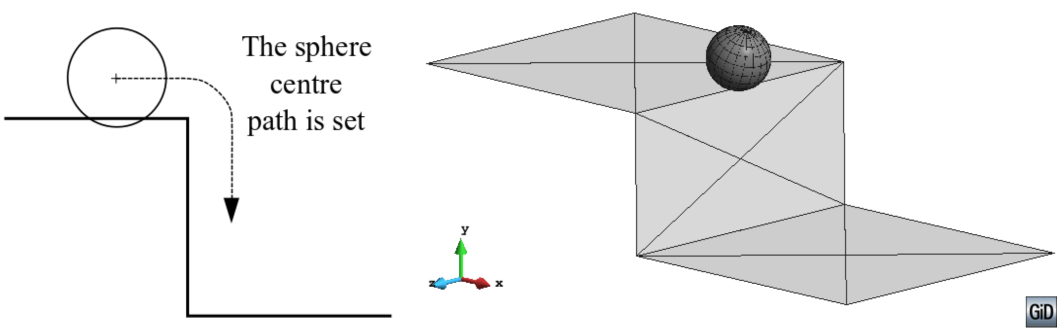

Figure 3.18: Simulation scheme.

If continuity is met, force module must always be the same. When the contact is with the surface, the direction of the force is equal to the normal of the plane and when the contact is with the axis the direction of the force is to the same direction as the vector that joins the axis and the centre of the sphere.

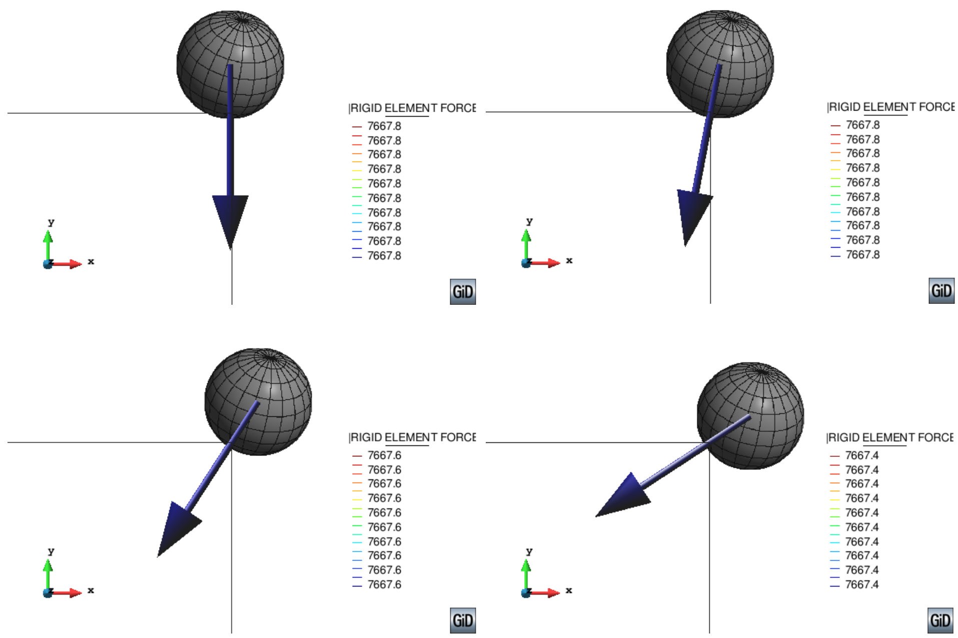

Figure 3.19: Force applied by the sphere to the surface and the axis at different instants of the simulation.

It is found that the results are as expected: no discontinuities arise when the contact changes from being with a surface or with an axis. The variation in the contact force module is less than 0.006%, thus negligible.

4 APPLICATIONS

4.1 Lateral resistance

4.1.1 Laboratory test

In 1997, Zand and Moraal [62] conducted a series of full-scale three-dimensional ballast resistance tests using a rail track panel. Those tests were performed in the Roads and Railways Research Laboratory of the Delft University of Technology (TU Delft).

The tests, whose layout is presented in Figure 4.1, consist of a track panel with five sleepers inside a ballast bed. Lateral load is introduced by means of two diagonal rods connecting the hydraulic actuator (150 kN) to the track section. Two connecting beams are welded between the rails to reinforce the track panel enabling a more uniform load introduction. The controlled variable is the velocity of the track panel inside the ballast bed, measuring the opposing force.

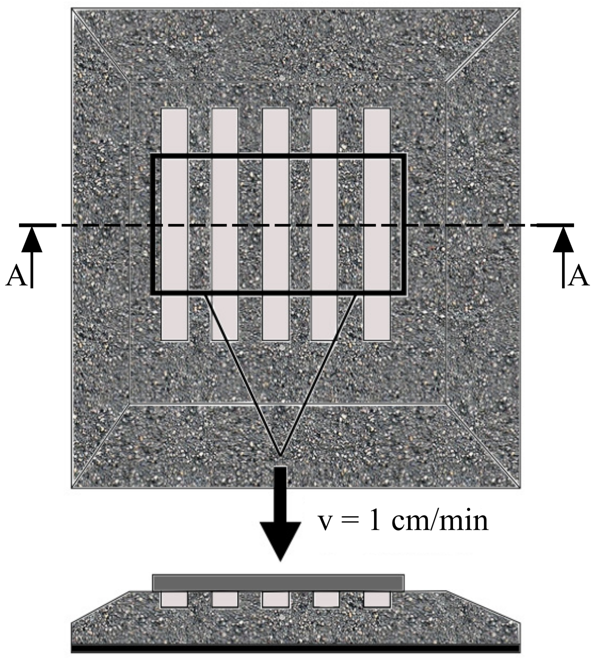

Figure 4.1: Laboratory test layout.

The laboratory tests were performed for different vertical loads applied on the track by dead weight existing of concrete slabs (with dimensions 2 m x 1.5 m x 0.01 m), weighing 9.95 kN each. In this work, the test with unloaded sleepers has been chosen for the simulations.

4.1.2 DEM simulation

The purpose of current work is to reproduce the laboratory test presented above. To that end, some calibration and validation simulations have been carried out, in order to understand properly the phenomenon.

The geometry for the simulations is the same as in the laboratory test, but for only one sleeper, instead of five. The geometry of the simulation is described in Figure 4.2. Lateral resistance test simulations have been developed using spherical discrete elements with rolling friction, the initial sphere mesh is shown in Figure 4.3.

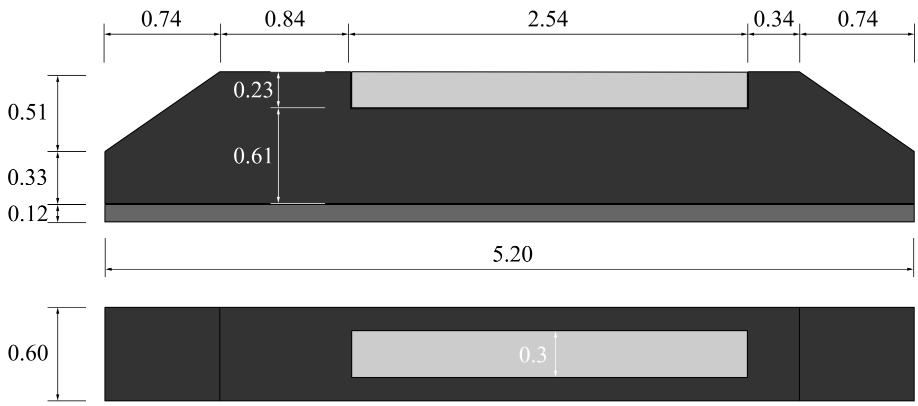

Figure 4.2: Test geometry for calculating ballast lateral resistance force against sleeper movement (distances in meters).

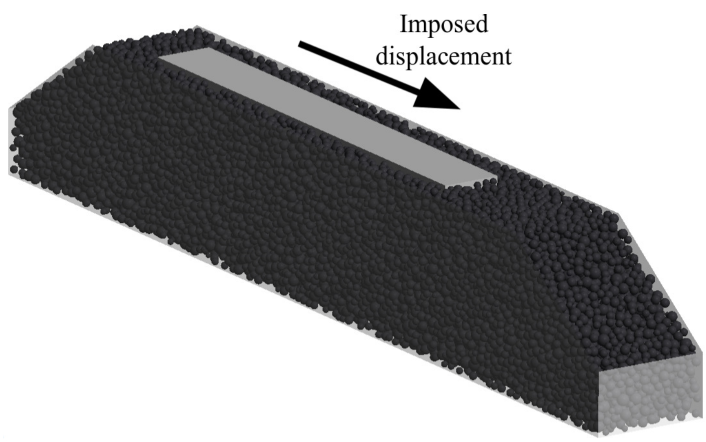

Figure 4.3: Initial sphere mesh used in the simulation for calculating ballast lateral resistance force against sleeper movement.

As a starting point, some reference data has been defined from literature. Table 4.1 summarizes the initial condition parameters.

- Ballast density: is one of the easiest parameters to defined. Ballast density used to be about 2700 (kg/m^3) [38], [44].
- Young modulus: according to Farmer [19], the Young modulus of most rock materials ranges from 2 to 9 GPa. The main problem of using such a high Young modulus value

is that, due to the explicit time integration scheme, the time step needed is too small. Therefore, the highest possible value that needed a reasonable time step was chosen for the first approaches, $1.2 \cdot 10^8$ Pa. As contacts are simulated as springs, the use of smaller rigidity will result in a larger indentation, but the macroscopic results will not be affected, provided that the indentation is moderate [53].

- Poisson ratio: Farmer [19] found that the Poisson ratio of most rocks was close to 0.2. According to Melis [44] ballast Poisson ratio is about 0.18.
- Mean diameter: in section 2.1.5 the mean diameter of railway ballast was defined (0.05 m).
- Friction coefficient between ballast stones: although this parameter depends on time and load cycles suffered by ballast stones, Melis [44] studied that the friction angle should always be between 30°and 40°(friction coefficient between 0.577 and 0.839).
- Friction coefficient between stones and sleeper: in section 2.1.5 an approximate value of this property was presented. It should be about 0.7.
- Restitution coefficient: Abellán [1] studied the restitution coefficient of such materials concluding that it is about 0.4.
- Rolling friction coefficient: no estimations of rolling resistance was found, as it is not a material property. Some previous calibration calculations for other materials has led to conclude that, for a sharp granular material like ballast, an appropriate value can be about 0.3 [27].

Table 4.1: Ballast properties for lateral resistance simulations (reference data).

Ballast density (kg/m^3)	2700
Young modulus (Pa)	$1.2 \cdot 10^8$
Poisson ratio	0.18
Mean diameter (m)	0.05
Friction coefficient between ballast stones	0.6
Friction coefficient between stones and sleeper	0.7
Restitution coefficient	0.4
Rolling friction coefficient	0.3

Regarding the definition of boundary conditions, friction between ballast and outer walls is considered null, as the domain is assumed to continue with mirrored particles.

4.2 Triaxial test

Large-scale triaxial tests, performed in the laboratory under controlled monotonic and repeated loading conditions, are commonly considered the best means to measure macroscopic mechanical properties of ballast materials [51]. The tests are carried out at a constant confining pressure, which simulates the mean pressure due to geostationary stresses in a railway structure [58], [5], [6].

Previous research on numerical modelling of ballast large-scale triaxial tests have focused on conducting simulations of aggregate particle assemblies using the DEM, trying to address the particulate nature of ballast material. These studies used spheres, cluster or polyhedral particles to model ballast stones [26], [43]. However, confining pressure has been applied through rigid elements or by numerical approximations, not representing the outer membrane, used in laboratory tests, with elastic membrane finite elements.

This section presents the development of a ballast discrete elements simulation approach, coupled with finite elements, for modelling ballast shear strength behaviour from large-scale triaxial compression tests.

4.2.1 Laboratory test

The reference triaxial test was performed in a large-scale triaxial compression test device developed at the University of Illinois for testing specifically ballast size aggregate materials (see Figure 4.4).

Figure 4.4: Large-scale triaxial compression test device developed at the University of Illinois. Source: Qian et al.[51]

The test sample dimensions are 30.5 cm in diameter and 61.0 cm in height. The acrylic test chamber is made of high strength glass fibre with dimensions of 61.0 cm in diameter and 122.0 cm in height. An internal load cell (Honeywell Model 3174) with a capacity of 89 kN is placed on top of the specimen top platen. Three vertical Linear variable differential transformers (LVDTs) are placed around the cylindrical test sample at 120-degrees angle between each other to measure the vertical deformations of the specimen from the three different side locations. Another LVDT can be also mounted on a circumferential chain wrapped around the specimen at the mid-height to measure the radial deformation of the test sample [51].

In the laboratory, different monotonic loading triaxial compression tests were conducted at three different confining pressures, at 68.9 kPa, 137.8 kPa, and 206.7 kPa in displacement control mode. The ballast strength tests were conducted at two different loading rates; slow conventional and rapid traffic induced. The shearing rate for the slow conventional strength test was adopted as 1% strain per minute, corresponding to 0.1016 mm/s, which is a common triaxial test shearing rate in the standard soil mechanics or geotechnical engineering practice. However, based on [22], rapid shear tests were performed moving up the ram to a maximum displacement of 38 mm/s, to evaluate strength properties of granular materials under transportation vehicle loading at rather rapid monotonic loading rates.

In this study, due to the computational demand of such a numerical model (sphere clusters for DEM calculation coupled with finite elements), only one laboratory test will be reproduced with confining pressure equal to 68.9 kPa and shear velocity equal to 38 mm/s.

An aluminium split mould was used to prepare the ballast test samples. Three layers of a latex membrane, with a total thickness of 2.3 mm, were fixed inside the split mould and held in place by applying vacuum to prepare each specimen in layers. A thin layer of geotextile was placed on top of the base plate to prevent clogging of the vacuum pump. Ballast material was poured into the mould and compacted with an electric jack hammer. After compaction the test sample was checked for the total height and the levelling of the top plate. Figure 4.5 shows the aluminium split mould on the left and the compacted ballast sample on the right ready for triaxial testing.

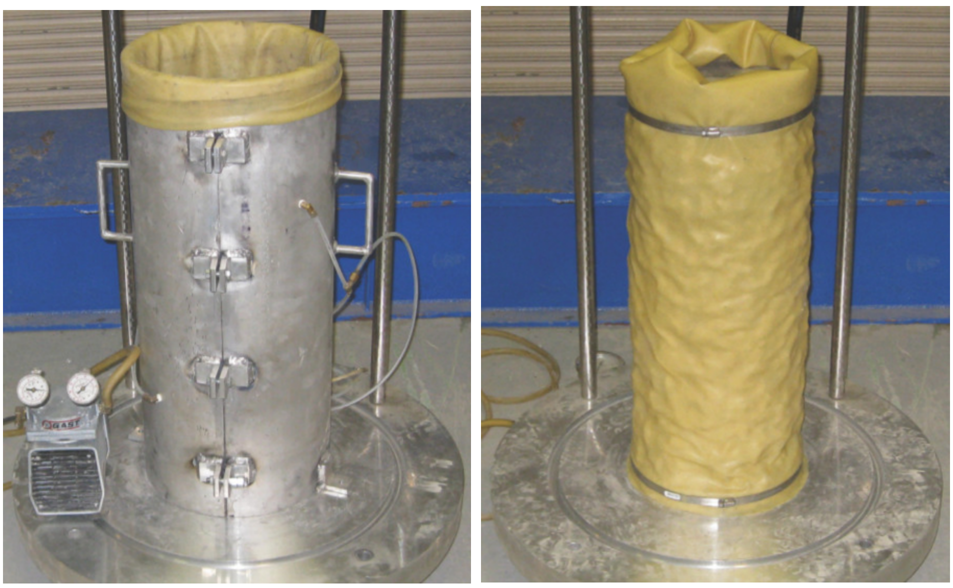

(a) Aluminium split mould. (b) Ballast test sample.

Figure 4.5: Large-scale triaxial test preparation. Source: Qian et al. [51].

4.2.2 DEM simulation

Section 3.2.2 defines the methodology followed to generate sphere clusters. Figure 4.6 shows the four different geometries chosen to represent ballast particles and the sphere cluster generated form each geometry.

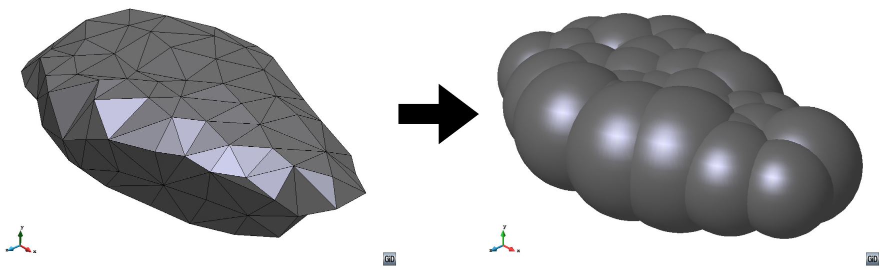

(a) Ballast cluster 1.

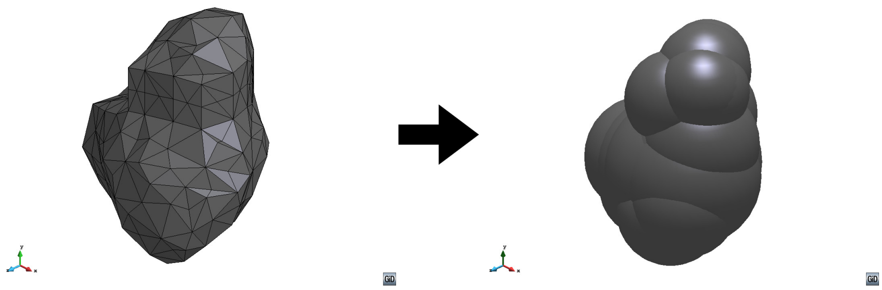

(b) Ballast cluster 2.

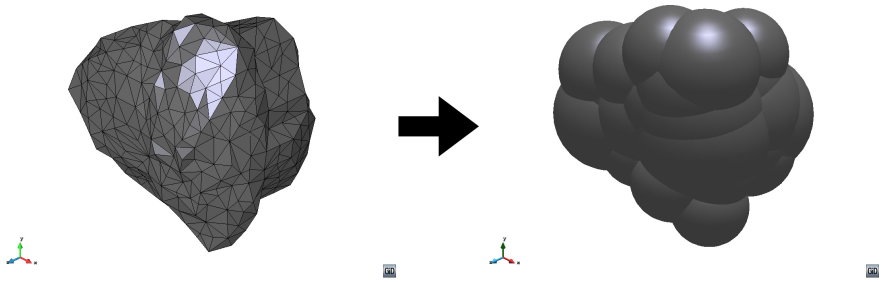

(c) Ballast cluster 3.

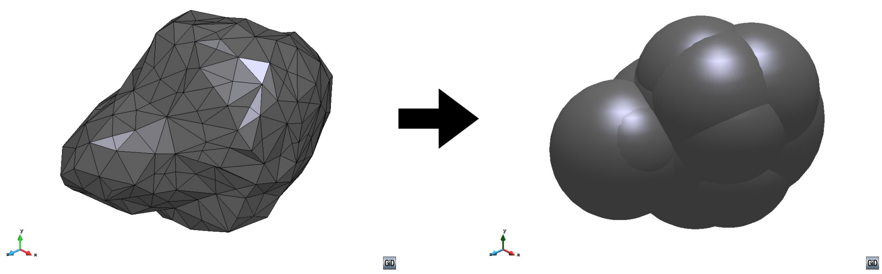

(d) Ballast cluster 4.

Figure 4.6: Initial geometry of the ballast particles chosen (left) and sphere cluster representation of those geometries (right). Red lines in the right image represent the initial width of the sample.

The clusters mesh was generated introducing the particles via, the so-called, *inlets*. Those inlets are predefined nodes, from which clusters are generated and introduced into the model, one by one with a determined velocity. The following steps summarize the model generation.

- Draw a rigid cylinder with the dimensions of the triaxial test utility. This would correspond to the aluminium split mould.
- Define the inlet nodes from which the particles will be introduced. The data needed is the position of the inlet, cluster geometric characteristics (cluster 1, 2, 3 or 4 and its orientation) and material properties.
- Start the simulation to introduce the particles via those inlets (Figure 4.7).

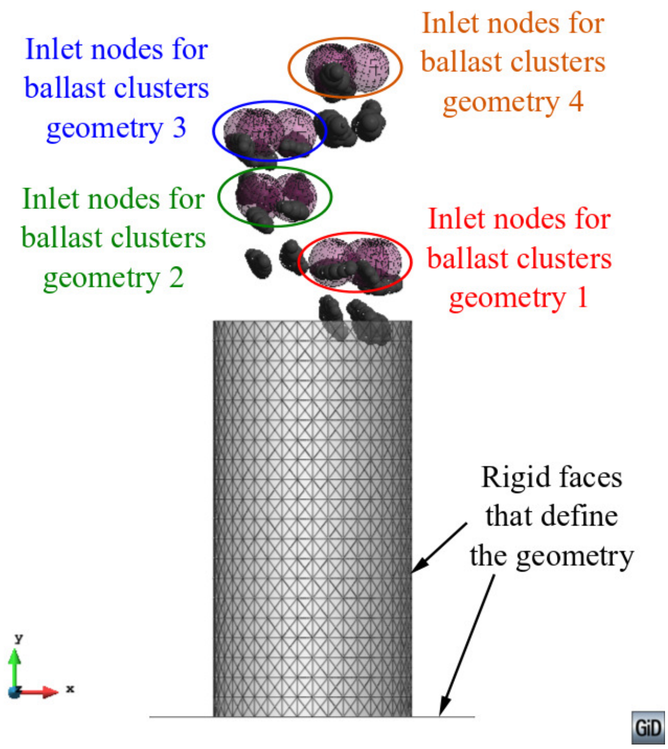

Figure 4.7: Particles inlet.

- Wait until all particles are introduced in the cylinder and rest. In this case particle introduction lasts 5 second, then the simulation takes other 5 seconds until the velocity of all particles is 0.
- Erase particles lying outside the cylinder domain. It is better to introduce more material than the necessary, in order to be sure that the cylinder is fulfilled.

In section 3.2.3, it has been proven that, with the method used for contact detection between discrete and finite elements, contact is totally smooth for rigid finite elements, but not for elastic finite elements. Figure 4.8 shows an scenario where the non-smooth contact detection introduces a calculation error. In Figure 4.8(a) the discrete element is in contact with an edge at time t, the indentation is δ and the contact force is F^t. At time $t + \Delta t$ (Figure 4.8(b)), the discrete element is in contact with two surfaces, because now the normal to those two surfaces is not the same. Since the time-step size, in explicit time integration algorithm, is usually very small, it is reasonable to suppose that the penetration vectors between the discrete element and surface 1 (δ_1) and surface 2 (δ_2) at time $t + \Delta t$ are similar to δ. Then the resultant contact is approximately: $\mathrm{F}^{t+\Delta t} = 2 \cdot \mathrm{F}^t$. Obviously, it can be concluded that the contact force is not smooth.

For quasi-static simulations with small time steps, the error introduced can be neglected [63]. Anyway, a new algorithm for the calculation of the contact force, based on the penetrated volume, is being developed. The computational cost of this new algorithm will be higher, that is why it should be evaluated when it will be worth using it.

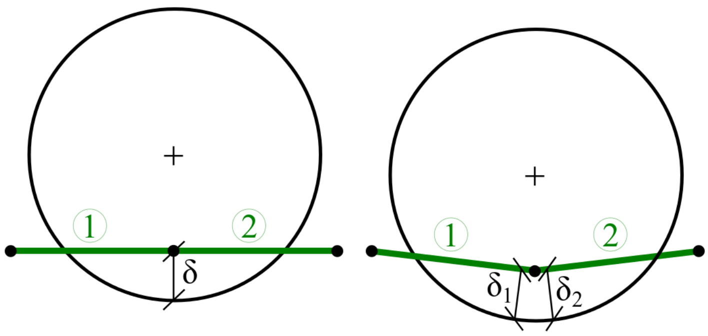

(a) Time t. (b) Time $t + \Delta t$.

Figure 4.8: Non-smoothness of the contact force with elastic elements. Source: Zang et al. [63].

Initial particle properties will be the same as for lateral resistance test, but in this case rolling friction should not be taken into account due to the fact that an approximation of the geometry is already considered. Now there are new properties that should be taken into account, which are membrane properties:

- Young modulus: According to Gere and Timoshenko [23], rubber Young modulus is between 0.7 and 4 $\cdot 10^6$ Pa. For this simulation, the value chosen is $1.5 \cdot 10^6$ Pa.
- Poisson ratio: The same authors established that rubber material Poisson ratio is between 0.45 and 0.5. The simulation has been carried out for a value of 0.45.
- Thickness: The membrane thickness of the laboratory test is 2.3 mm (section 4.2.1).
- Friction coefficient between stones and membrane: Qian et al. [51] considered friction between stones and membrane equal to 0. This assumption is based on the membrane deformation that meets perfectly ballast stones shape and the quasi-static nature of the experiment.
- Friction coefficient between stones and actuators: Liu [35] studied the repose angle of granular materials lying over surfaces of different materials. The friction angle between stones (similar to ballast) and a smooth material, like the actuators, is about 15°(which corresponds to a friction coefficient of 0.268).

Table 4.2 summarizes all the material properties of the simulations.

Table 4.2: Ballast and membrane properties for the large-scale triaxial test simulation (reference data).

Ballast	
Ballast density (kg/m^3)	2700
Young modulus (Pa)	$1.2{\cdot}10^8$
Poisson ratio	0.18
Mean diameter (m)	0.05
Friction coefficient between stones and membrane	0.0
Friction coefficient between stones and actuators	0.268
Restitution coefficient	0.4
Membrane	
Young modulus (Pa)	$1.5{\cdot}10^6$
Poisson ratio	$1.2{\cdot}10^8$
Thicness (m)	0.0023

When dealing with the large-scale triaxial test, a new problem has been found, derived from the different rigidity of the membrane and the ballast stones. Discrete element particles (ballast stones) stiffness is much higher than the stiffness of the membrane. This would lead to high contact forces in contacts with relatively low indentation, that could cause excessive deformations in the elastic membrane. One simple solution is the decrease of the time step, to stabilize the numerical model. If the necessary time step is too low, making the simulation time unapproachable, an alternative algorithm should be used. In this case, the solution chosen was a penalty algorithm [63].

Considering contact between discrete and finite elements and linear constitutive model, normal stiffness is calculated as:

$$k_n^{DEM} = \frac{E_{DEM}\pi r_i}{2}, \tag{4.1}$$

where E_{DEM} is the Young modulus of the discrete elements, and r_i is the radius of the discrete element particle.

Applying the penalty algorithm, normal stiffness is calculated as:

$$k_n^{FEM} = \gamma \frac{E_{FEM}\pi r_i}{2} \tag{4.2}$$

where γ is the penalty parameter, that should be calibrated in order to have an appropriate time step but not too much indentation. E_{FEM} is the Young modulus of the finite elements.

In the previous first simulations of the large-scale triaxial test γ was fixed to 10.

5 RESULTS AND DISCUSSION

5.1 Lateral resistance

This section is divided in three subsections. The aim of subsections 5.1.1 and 5.1.2 is to calibrate the model and try to understand better the governing mechanisms of the phenomenon. Subsection 5.1.3 presents the results obtained to date.

5.1.1 Material properties and input parameters influence

Firstly, the influence of some material properties and input parameters has been assessed, in order to evaluate suitable changes or simplifications. Table 5.1 summarizes the data used. Bold numbers represent the reference values, defined in Table 4.1.

Table 5.1: Data summary.

Material properties	
Friction coefficient between ballast stones	**0.6**/0.7/0.8/0.9
Friction coefficient between ballast and sleeper	0.6/**0.7**/0.8/0.9
Rolling friction coefficient	0.1/**0.3**
Restitution coefficient	0.2/**0.4**
Input parameters	
Sleeper velocity (m/s)	0.05/0.5
Particle stabilization time (s)	0.01/0.1
Sleeper load (N)	0/2000

The aim of this simulations is to understand the phenomenon, evaluating how does each parameter influences the system response, so, sleeper velocity used is very high compared to the laboratory test velocity, due to the fact that the objective of this simulations campaign is not reproducing exactly laboratory tests. The main reason to increase the velocity of the sleeper is the calculation time.

- **<u>Variation of the friction coefficient between ballast stones</u>:**

  The first parameter evaluated is the friction coefficient between ballast stones. The graph in Figure 5.1 shows the influence of the friction coefficient in the ballast lateral resistance. With larger friction coefficients, the lateral resistance increases. The same behaviour can also be observed in Figure 5.2.

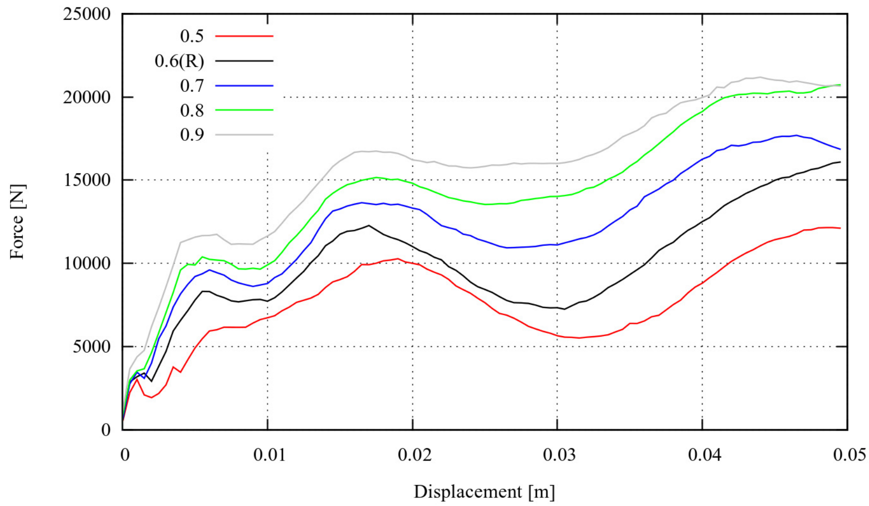

Figure 5.1: Obtained results varying friction coefficient between ballast stones.

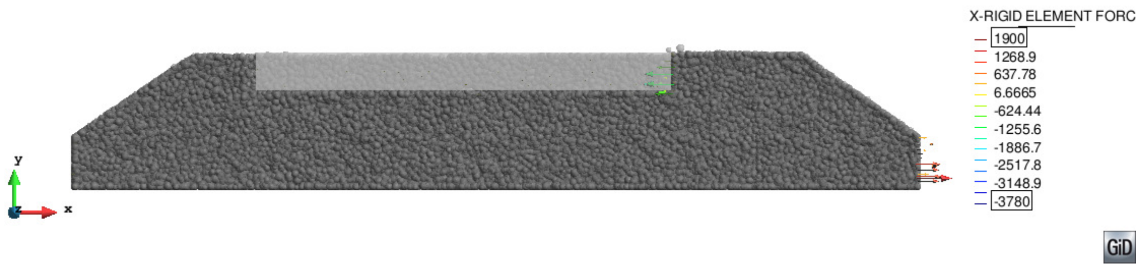

(a) Friction coefficient = 0.5.

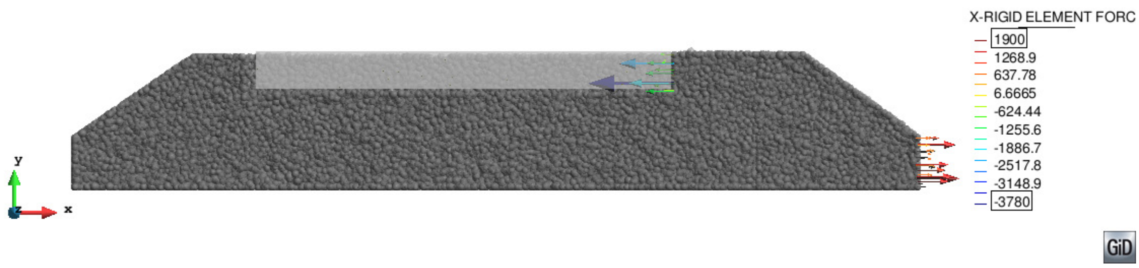

(b) Friction coefficient = 0.9.

Figure 5.2: Difference between two simulations when the sleeper has been moved 5 cm. It can be seen that lateral resistance increases with friction coefficient.

- **Variation of the friction coefficient between ballast and sleeper:**

  The influence of the friction coefficient between ballast and sleeper was also studied. Figure 5.3 shows that the influence of the friction coefficient between ballast and sleeper is important only at the beginning, when the sleeper has been moved a few millimetres. Then, the lateral force is dominated by the resistance of ballast shoulder, and not by friction between sleeper bottom part and ballast stones. Ballast force against sleeper movement, when the sleeper has been moved 3 mm, can be observed in Figure 5.4.

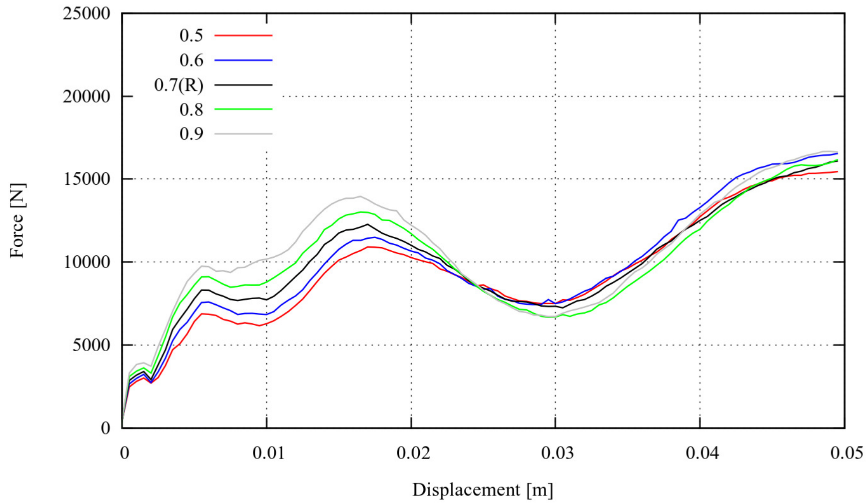

Figure 5.3: Obtained results varying friction coefficient between ballast and sleeper.

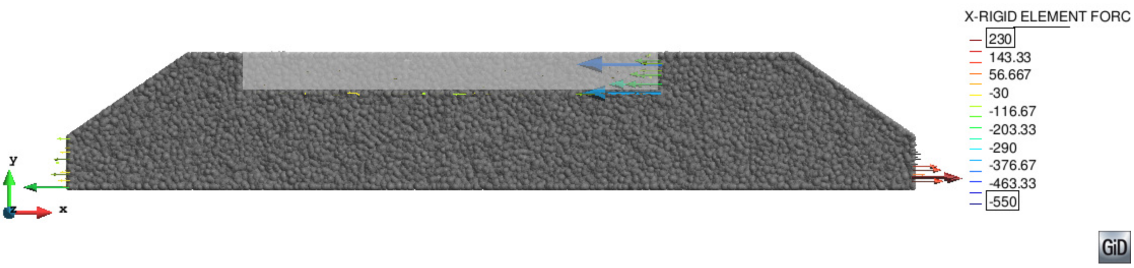

(a) Friction coefficient between ballast and sleeper = 0.5.

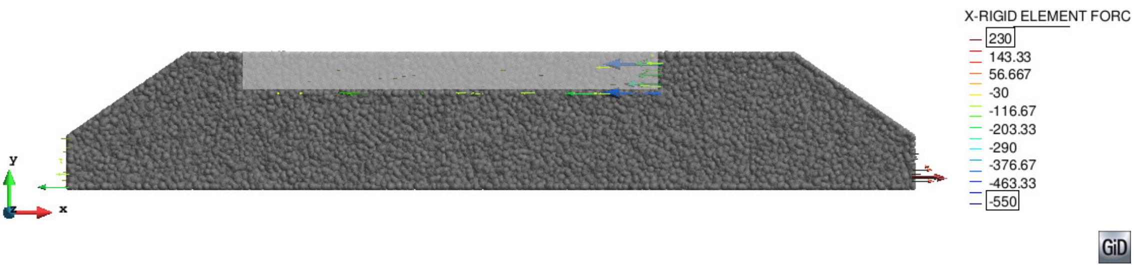

(b) Friction coefficient between ballast and sleeper = 0.9.

Figure 5.4: Difference between two simulations when the sleeper has been moved 3 cm. A higher coefficient of friction between ballast and sleeper increases the lateral force of the ballast at the bottom of the sleeper.

- **Variation of the rolling friction coefficient:**

  As rolling friction is not a material property, it is difficult to assign an appropriate value to it. What can be clearly seen in the graph of Figure 5.5 is that the lower the rolling friction coefficient is, the easier particles can rotate. In other words, lateral ballast resistance decreases with the decrease of rolling friction coefficient, as stones do not bear enough load without rotating.

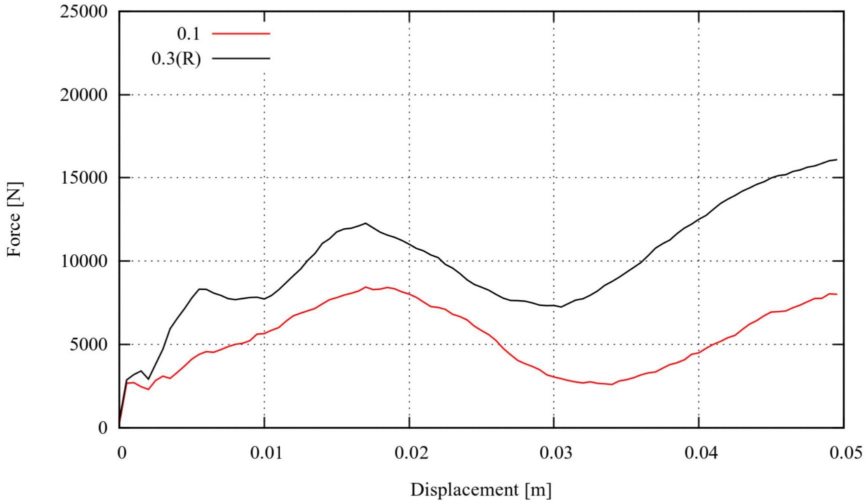

Figure 5.5: Obtained results varying rolling friction coefficient.

Figure 5.6 shows particles orientation when the sleeper has been moved 5 cm. It can be observed that for a value of rolling friction equal to 0.1 particles have rotated more than for a value of rolling friction equal to 0.3.

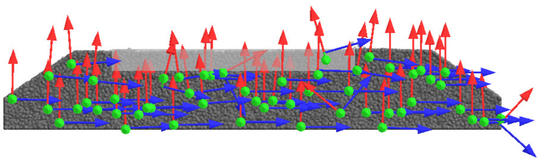

(a) Rolling friction coefficient = 0.1.

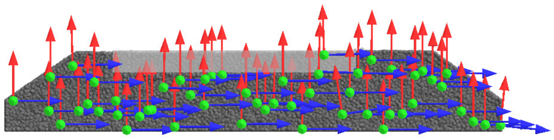

(b) Rolling friction coefficient = 0.3.

Figure 5.6: Particle rotation when the sleeper has been moved 5 cm for rolling friction coefficient values equal to 0.1 and 0.3.

- **Restitution coefficient variation:**

  The restitution coefficient of two colliding objects represents the ratio of speeds after and before an impact. Pairs of objects with restitution coefficient equal to 1 collide elastically, while if the restitution coefficient is smaller than 1 the collision is inelastic, in other words, energy is dissipated during the collision. Taking into account that this simulation is quasi-static, it can be assumed that the restitution coefficient should not affect the results because relative velocity between particles is low.

  Figure 5.7 shows that previous assumption is met and the variation of the restitution coefficient is not affecting the results significantly.

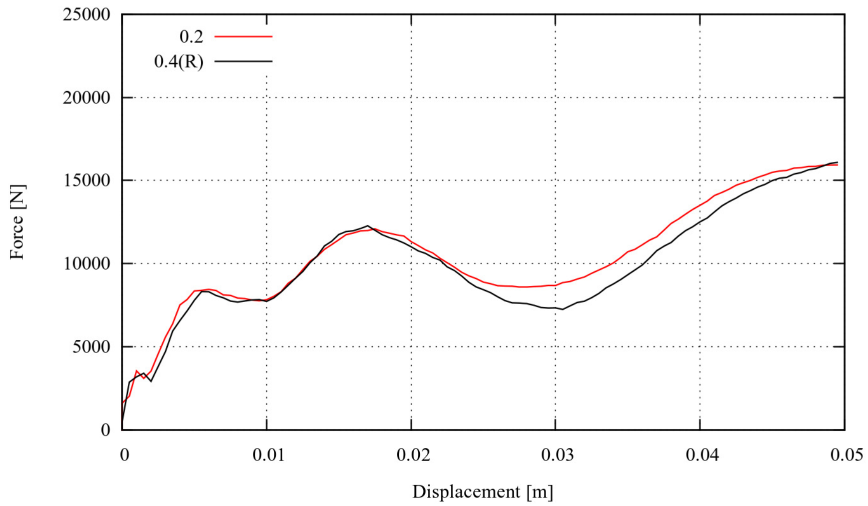

Figure 5.7: Results obtained by varying the restitution coefficient.

The above tests have not already proven the correctness of the method for the calculation of ballast response, but it is demonstrated that it is a very interesting tool to evaluate the influence of different parameters, something very difficult to determine with laboratory tests. It also presents other advantages, for example, the possibility of displaying the force applied by each stone against sleeper movement, almost impossible to know with a simple on-site test.

- **Variation of the sleeper velocity:**

  The influence of the sleeper velocity in the lateral ballast resistance has also been tested. Figure 5.8 clearly shows that the change in sleeper velocity over the ballast bed affects the system response. When the sleeper is moved faster, particles do not have time to relocate, so force increases or decreases depending on the stones arrangement. When the velocity is lower, the system can be relocated, allowing lateral resistance stabilization once it has reached the maximum.

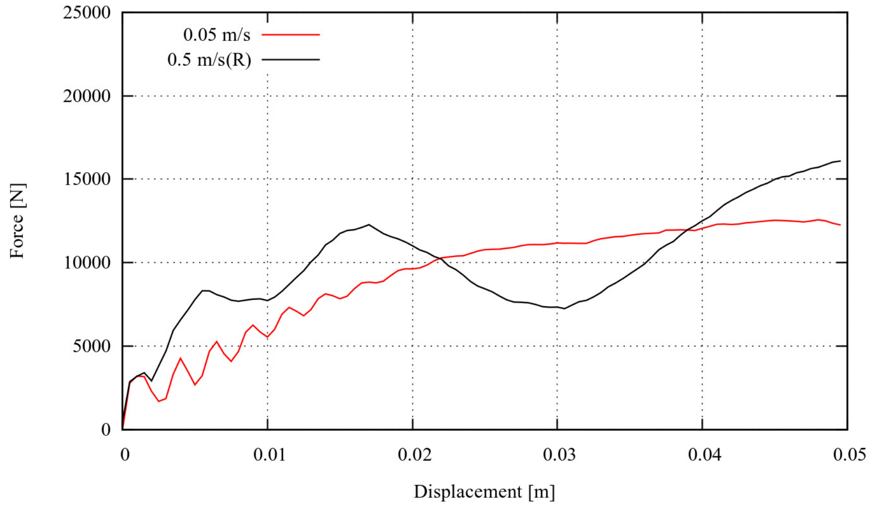

Figure 5.8: Obtained results varying the sleeper velocity.

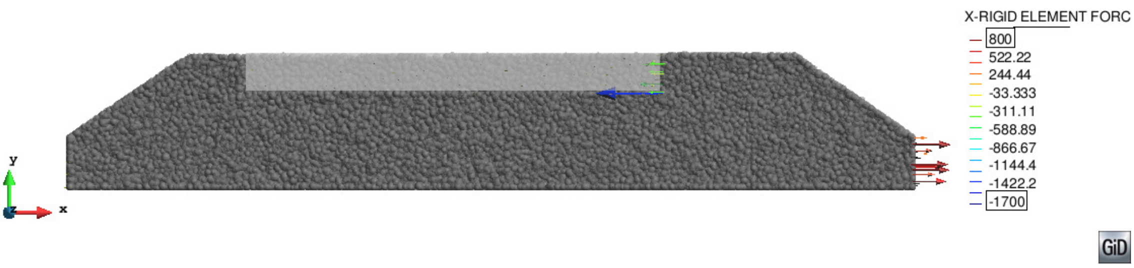

(a) Sleeper velocity = 0.05 m/s.

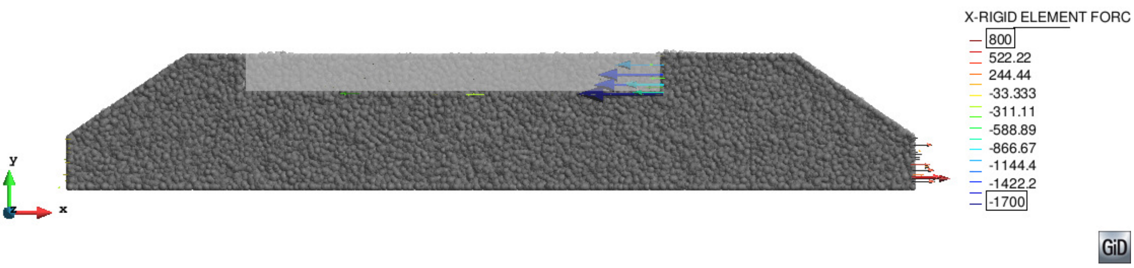

(b) Sleeper velocity = 0.5 m/s.

Figure 5.9: Difference between two simulations, when the sleeper displacement is 1.75 cm. The lateral force increase, when sleeper velocity is greater, can be observed.

- **<u>Particle stabilization time influence</u>:**
Stabilization time is the time before the sleeper starts moving. This parameter is important because when the simulation starts, particles were arranged depending on the sphere-mesher. During the first time steps, stones and sleeper move until they reach their rest position. Graph in Figure 5.10 shows the influence of this parameter.

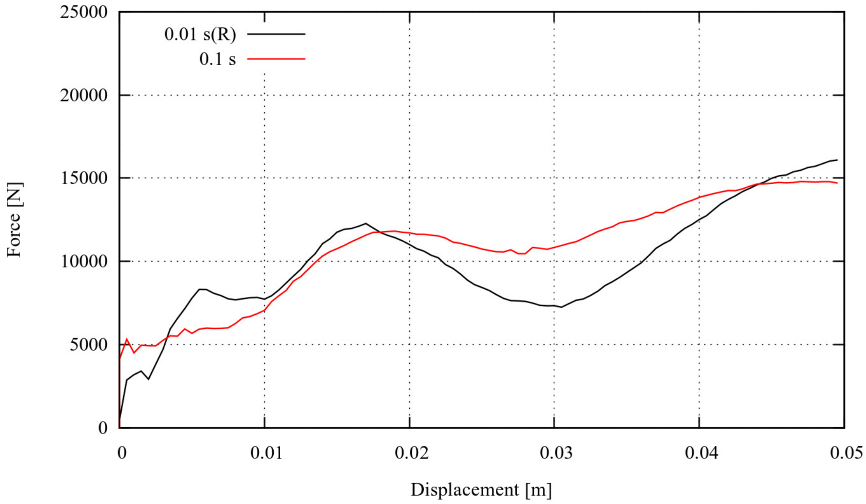

Figure 5.10: Results obtained by varying the stabilization time.

As in the case in which the speed of the sleeper is changed, the initial stabilization time greatly affects the results. It can be concluded that the arrangement of ballast stones is an important factor that influences the final results. When the stabilization time is higher, the lateral resistance of the track is more stable.

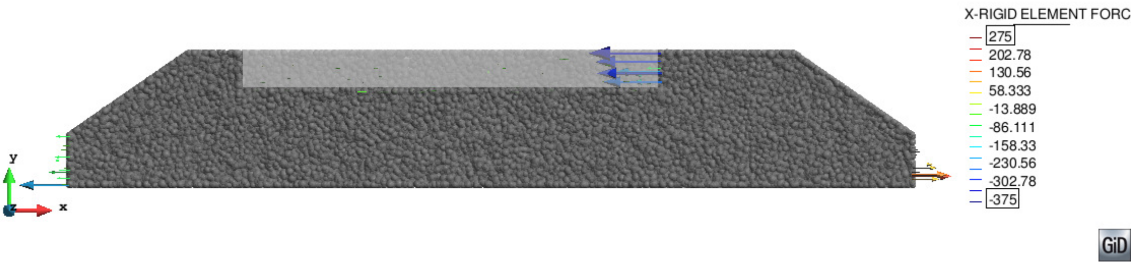

(a) Stabilization time = 0.01 s.

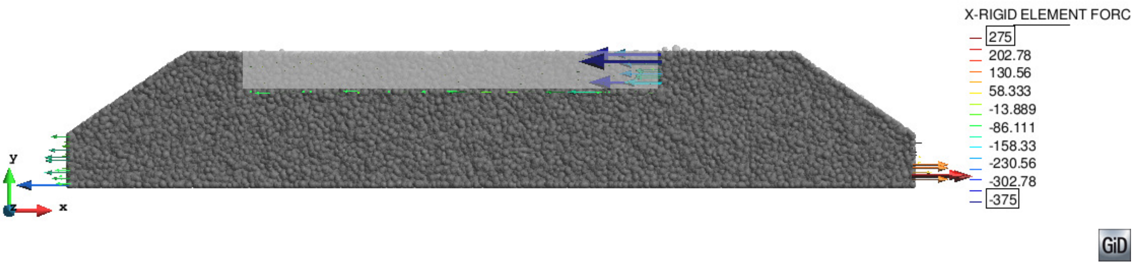

(b) Stabilization time = 0.1 s.

Figure 5.11: Difference between two simulations, when the sleeper displacement is 0.5 mm. Increasing the stabilization time implies a more stable arrangement of particles, leading to an increase of the friction of the bottom of the sleeper because the contact surface also increases.

- **Sleeper load influence:**

  The load on the sleeper in the reference test is null, which means that the only vertical load applied is the self-weight. In this case, European concrete sleepers and rails have been considered, weighting 3720 N. The graph in Figure 5.12 shows how the load over the sleeper affects the system response. When the sleeper is loaded (in this case 20000 N) the lateral resistance of the track depends largely on the friction of the bottom of the sleeper with ballast stones, while when it is unloaded the prevailing phenomenon is ballast shoulder resistance.

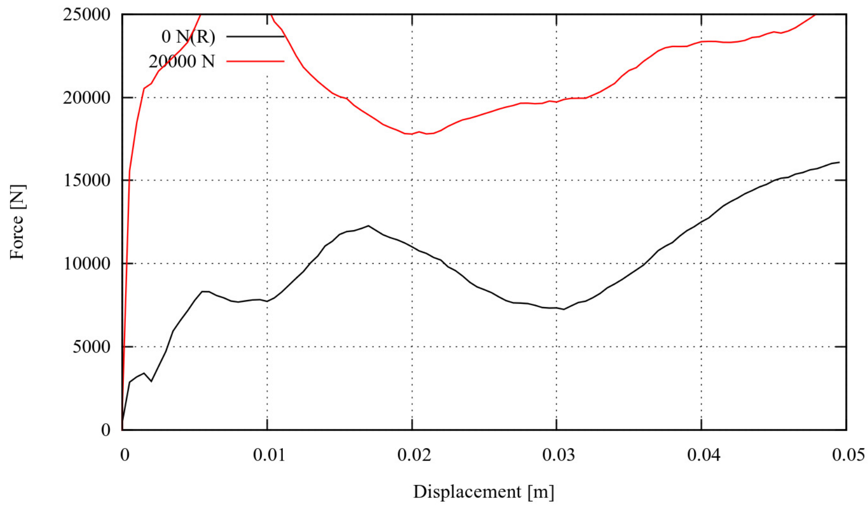

Figure 5.12: Results obtained by varying the vertical load imposed on the sleeper.

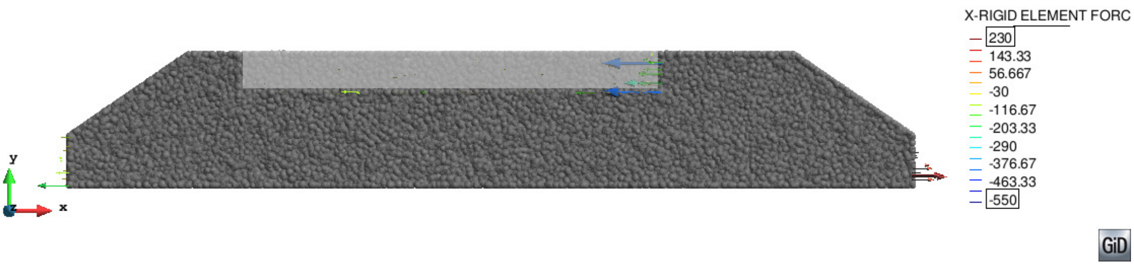

(a) Unloaded sleeper.

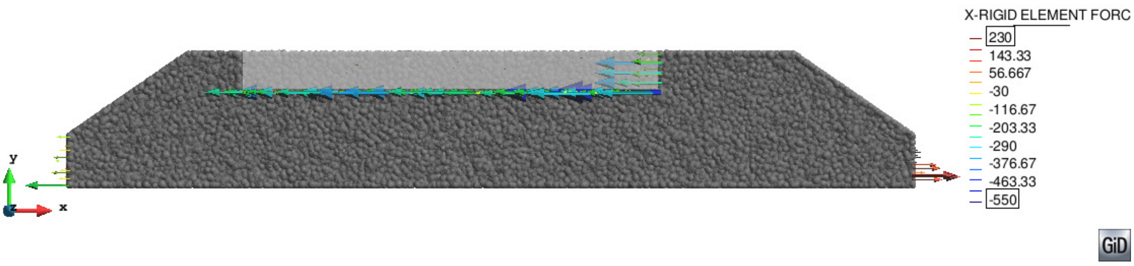

(b) Loaded sleeper.

Figure 5.13: Difference between two simulations when the sleeper has been moved 0.5 mm. Vertical load increase implies more friction between ballast stones and the bottom part of the sleeper.

5.1.2 Laboratory test

The above mentioned simulations evaluate most of the parameters involved in the calculation and improve the understanding of the phenomenon. After that, the laboratory test has been reproduced. The simulation material properties and input parameters are presented in Table 5.2.

Table 5.2: Material properties and input parameters for laboratory lateral resistance simulation.

Ballast properties	
Ballast density (kg/m^3)	2700
Young modulus (Pa)	$1.2 \cdot 10^8$
Poisson ratio	0.18
Mean diameter (m)	0.05
Friction coefficient between ballast stones	0.6
Friction coefficient between stones and sleeper	0.7
Restitution coefficient	0.4
Rolling friction coefficient	0.3
Input parameters	
Sleeper velocity (m/s)	0.01
Stabilization time (s)	1.0

Although sleeper velocity is not the same as in the laboratory test (due to available time issues), the chosen value is considered to be low enough to provide stable results.

Graph of Figure 5.14 compares laboratory results with those obtained in the simulation. It can be seen that the numerical model calculates correctly the maximum lateral resistance (about 9500 N), but the slope of the curve (stiffness) at the beginning is much lower in the simulation than in the laboratory test.

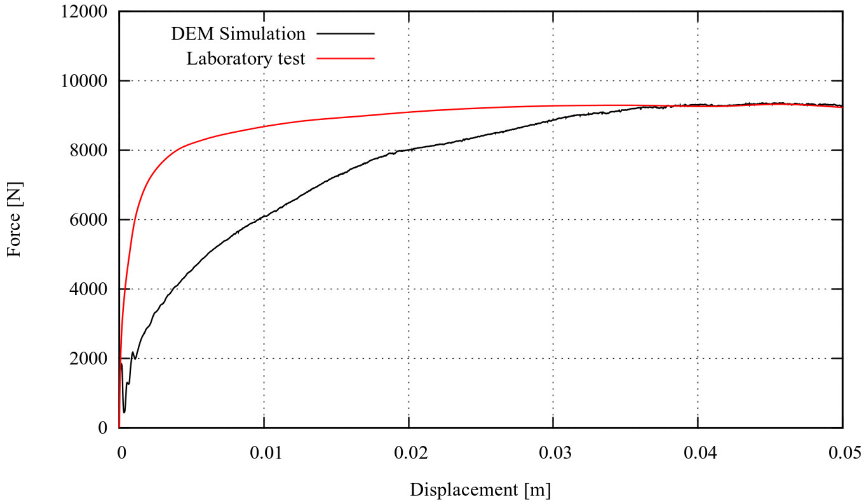

Figure 5.14: Comparison of the lateral force applied by ballast stones against sleeper movement between laboratory test and numerical model simulation.

The maximum lateral resistance is calculated correctly, but there are still differences in the obtained curve. Therefore, some slightly modifications will be developed.

The material properties and the input parameters of the following simulations will be those presented in Table 5.2. In those simulations some geometry changes will be developed in order to compare the system response and look for the source of error.

- **Ballast box vibration**:

  In this case, the sleeper starts moving after the box has been vibrated (Figure 5.15). The objective of this vibration is the rearrangement of ballast stones into a more stable position, aiming to increase the lateral resistance stiffness. This operation is similar to tamping operation, carried out in all railway ballast tracks. In the simulation without vibration, the stabilization time is 1 second, while in the simulation after vibration, the box vibrates 0.5 seconds and then the stabilization time are other 0.5 seconds.

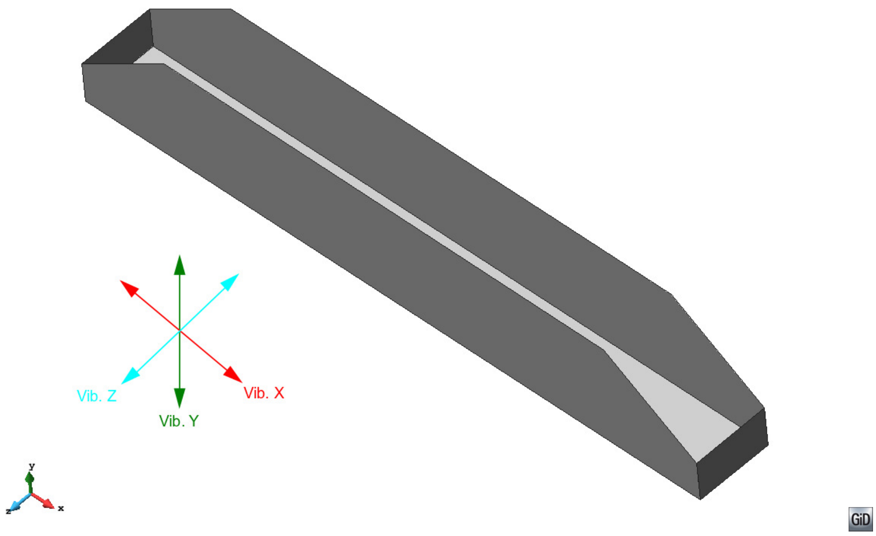

Figure 5.15: Box vibration.

Figure 5.16 shows the comparison between the simulation without vibration (graph in Figure 5.14) and the simulation after box vibration.

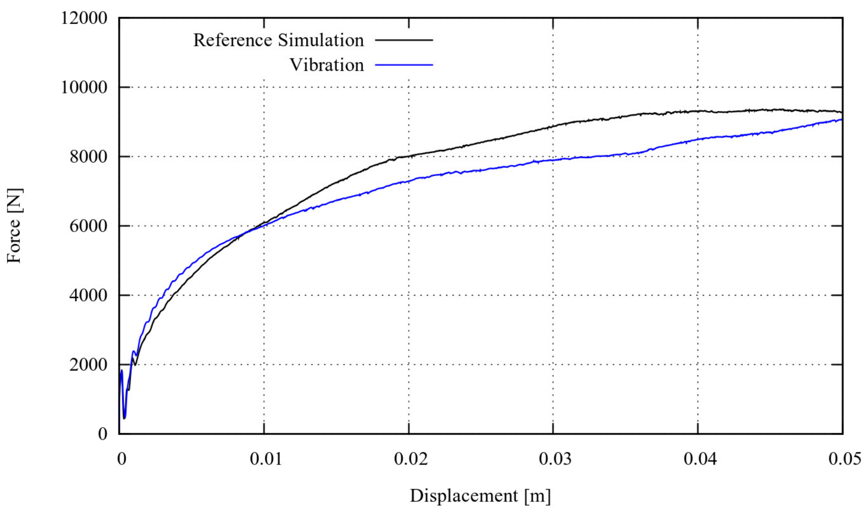

Figure 5.16: Comparison of results obtained in vibrating and no vibrating simulations.

From the results, it can be concluded that ballast stones vibration for better rearrangement does not improve system response in the expected way.

- **Calculation in a bigger domain:**

  To check if the boundary conditions imposed are a source of error, the ballast domain has been increased. Figure 5.17 shows the difference between the standard domain and the new bigger domain.

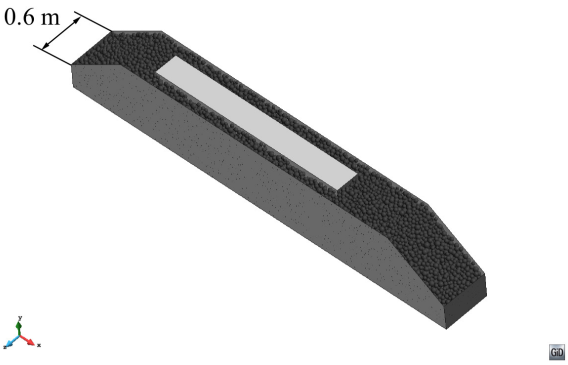

(a) Standard geometry.

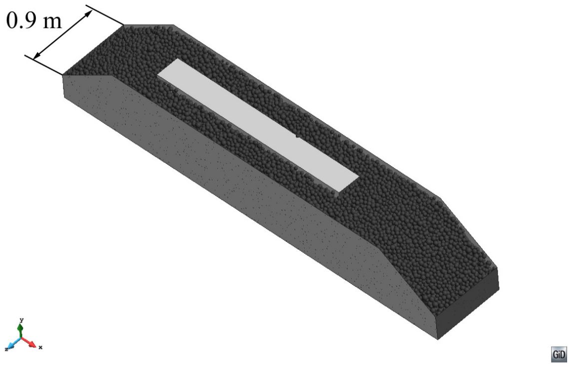

(b) Bigger domain.

Figure 5.17: Difference in lateral force between both ballast domains.

The results comparison is shown in Figure 5.18.

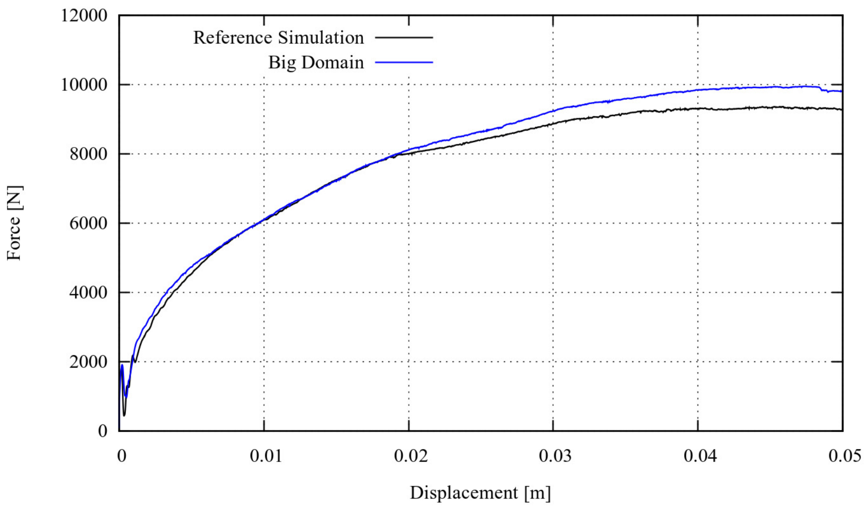

Figure 5.18: Comparison of results obtained with ballast domain width 0.6 m and 0.9 m.

From the results, it can be concluded that the boundary conditions imposed are not a source of the error. Lateral force at the beginning is almost the same in both cases. When the sleeper has moved more than 2 cm some differences start to appear, something expected, as there is more material in the ballast shoulder when the domain is bigger.

- **Calculation of the contribution of each part to the total lateral resistance:**

  To better understand the contribution of each resistant element (sleeper bottom friction, sleeper lateral friction and ballast shoulder) to global lateral resistance, independent simulations, to evaluate the contribution of each section, have been developed.

  Figure 5.19 shows the geometries used to evaluate the contribution of each of part to the whole lateral resistance.

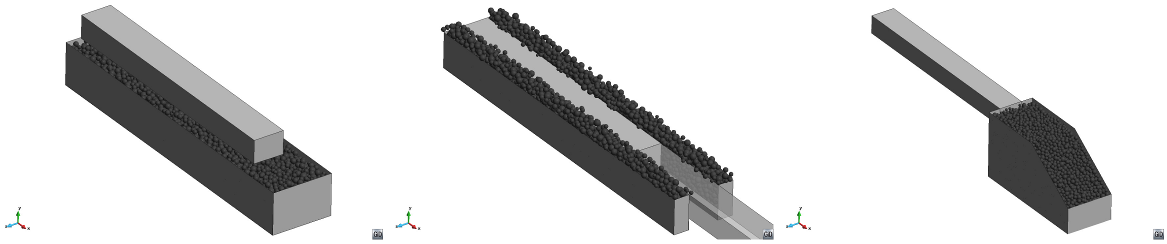

(a) Sleeper bottom part friction. (b) Sleeper side walls friction. (c) Resistance of ballast shoulder.

Figure 5.19: Geometries used to determine the contribution of each of the resistant parts to the whole lateral resistance.

The obtained results are displayed in the graph of Figure 5.20. From those results it can be concluded that the lack of stiffness is due to the resistance of the ballast shoulder (the slope of the curve is very small), since the force applied to the side walls and the bottom of the sleeper increases very fast at the beginning and then remains constant. The shoulder resistance is increasing during the first 5 cm of movement of the sleeper. It should also be noted that, the sum of the lateral resistance force of each section is close to the lateral resistance force obtained in the global geometry simulation (see Figure 5.14, about 9500 N).

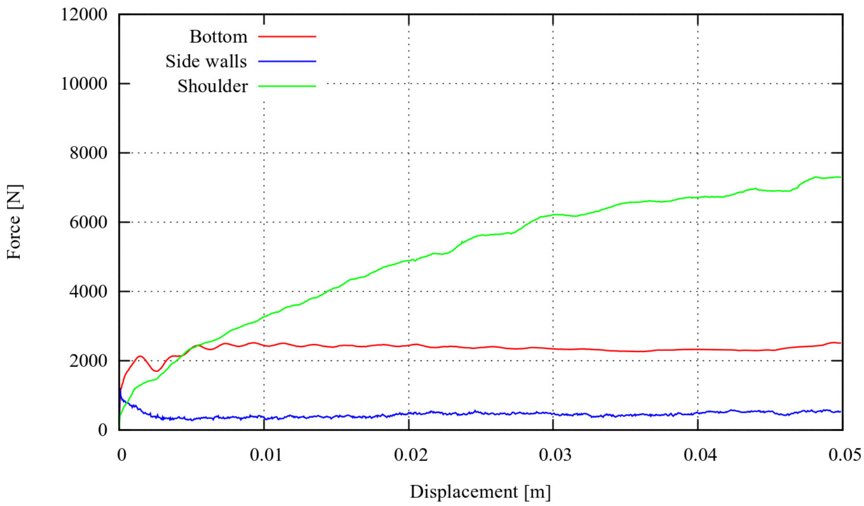

Figure 5.20: Lateral resistance provided by the bottom of the sleeper, the side walls of the sleeper and the ballast shoulder.

5.1.3 Current results

Stiffness and mesh influence

From section 5.1.2, it can be concluded that the main problem of the simulation is the shoulder rigidity. For that reason, the next developed simulation was performed changing ballast stiffness, although it leads to a lower time step, in other words, a higher calculation time.

Other possible change would be the particles distribution. Tran [59] proposed an appropriate technique in order to generate discrete elements samples for granular material simulations. Till this point, the meshes used were generated by the meshers available in *GiD* (`www.gidhome.com/support/manuals`). Those meshers provide good particles distributions for cohesive material, but for discrete materials the packing factor is low.

The packing method finally chosen is, the so-called, gravitational packing technique, and it was developed as follows:

- A geometry, bigger than the geometry occupied by the granular material should be drawn. In this case, ballast layer was increased 17.5 cm, as shown in Figure 5.21.

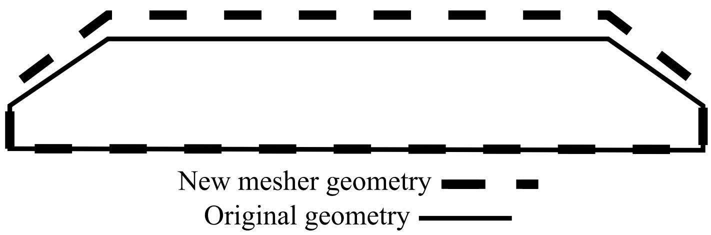

Figure 5.21: Original ballast geometry compared to the ballast geometry used to perform the new spheres mesh.

- A sphere particle mesh is generated in the new geometry, using the radius expansion method, available in *GiD*.
- Ballast material properties should be assigned to the particles, but with a very important change, their friction coefficient should be 0. The reason to use that unrealistic value for the friction coefficient is that it would allow the particles to be placed in the most packaged manner. After meshing operation, before the real simulation starts, ballast particle friction would be reassigned to 0.6.
- During the meshing simulation some surfaces were used as a cover (see Figures 5.22 and 5.23) to obtain the intended geometry. As friction coefficient between particles is 0, the repose angle would be also 0, that means that the lateral ballast slopes will disappear, and that is why the cover is needed. In this point, it is important to remark that the force over the top part of the cover should be 0, otherwise, some particles should be deleted to avoid compression which would distort results.
- The particles need some time to reach the rest position, once this position is reached the mesh is obtained.

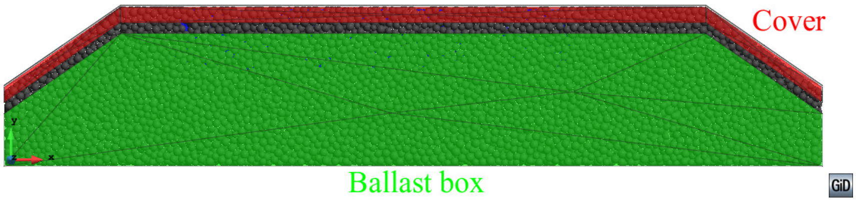

(a) View XY plane.

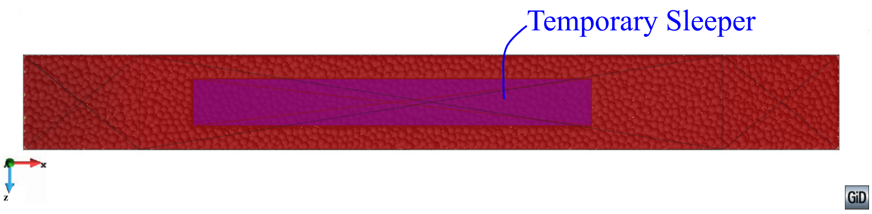

(b) View XZ plane.

Figure 5.22: Initial geometry for the elaboration of the sphere mesh.

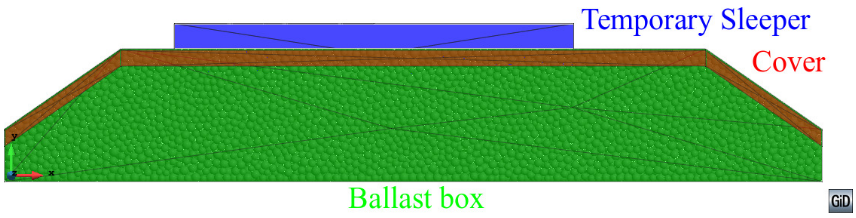

(a) View XY plane.

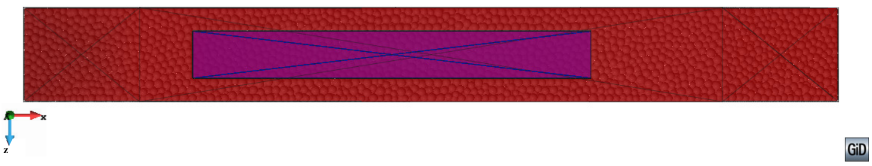

(b) View XZ plane.

Figure 5.23: Final position of the spheres without friction.

The data used in the new simulation, with the particles distribution obtained via the gravitational packing technique, is summarized in Table 5.3. It can be seen that, as it was already commented, the material stiffness has been increased compared to previous simulations. The material Young modulus chosen is $5.1 \cdot 10^9$ Pa, inside the range established by Farmer [19] for rock materials (between 2 to 9 GPa, see section 4.1.2). In this case, sleeper velocity is the same as in the laboratory test.

Table 5.3: Ballast properties and input parameters for the calculation of ballast lateral resistance.

Ballast properties	
Ballast density (kg/m^3)	2700
Young modulus (Pa)	$5.1{\cdot}10^9$
Poisson ratio	0.18
Mean diameter (m)	0.05
Friction coefficient between ballast stones	0.6
Friction coefficient between stones and sleeper	0.7
Restitution coefficient	0.4
Rolling friction coefficient	0.3
Input parameters	
Sleeper velocity (m/s)	0.0001667
Stabilization time (s)	1.0

Results obtained with the new mesh

Graph in Figure 5.24 shows the results obtained with the *DEM-application* compared to laboratory data.

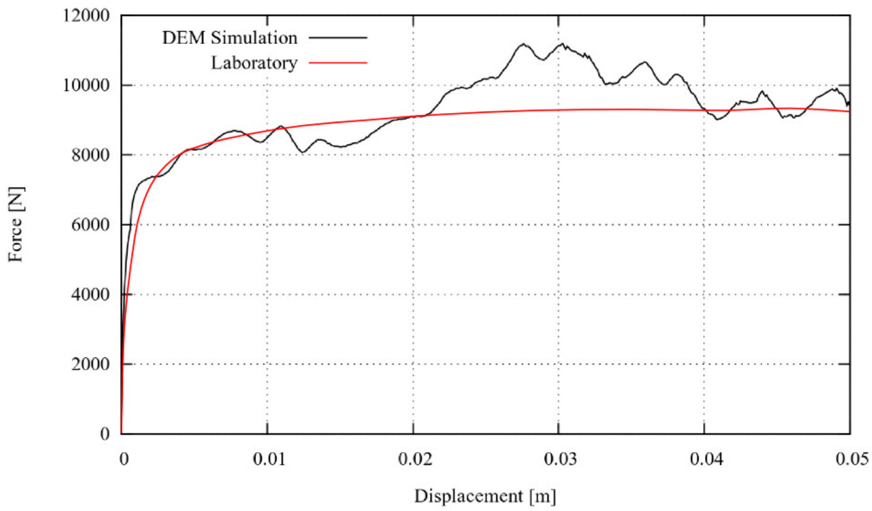

Figure 5.24: Comparison between results obtained with the *DEM-application* and laboratory tests.

It can be seen that, in this case, the initial resistance stiffness is correctly captured by the numerical model. The maximum lateral resistance is overestimated in the numerical model. Future work will be in the way of decreasing the time step and trying with the Hertz constitutive model. Notwithstanding the remaining errors, it can be said that the *DEM-application* is an appropriate tool to calculate ballast response against sleeper movement.

Figure 5.25 shows the lateral force applied by each particle against sleeper displacement when the sleeper has been moved 2 mm.

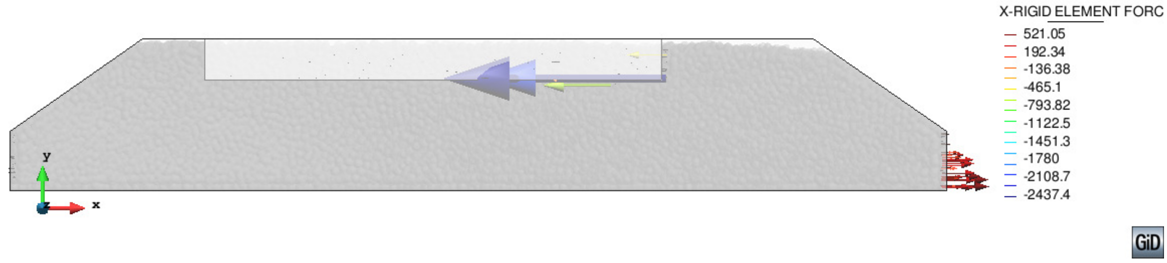

Figure 5.25: Ballast particles lateral force against sleeper displacement when the sleeper has been moved 2 mm.

Figure 5.26 shows the ballast particles lateral displacement when the sleeper has been moved 5 cm.

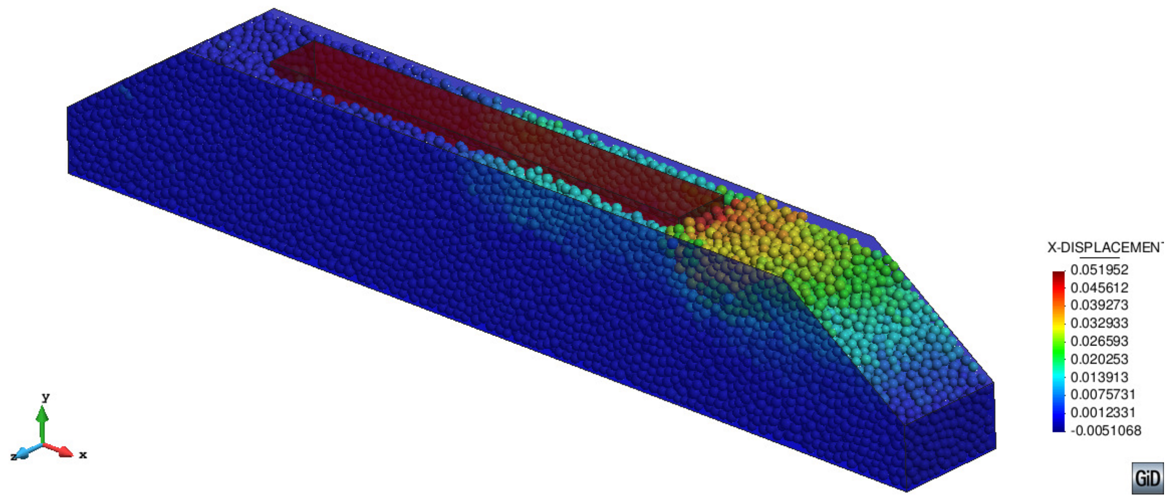

Figure 5.26: Ballast particles lateral displacement when the sleeper has been moved 5 cm.

5.2 Triaxial test

Although, for the first simulations the data chosen was the specified in section 4.2.2, the conclusions drawn after the lateral resistance calculations, about meshing and ballast stiffness, led to some changes.

Table 5.4 shows the material properties after the changes derived from the lateral resistance tests. It should be noted that, as the ballast stiffness has been changed, the penalty factor (γ), for contact between discrete and finite elements, has also been changed from 10 to 100.

Table 5.4: Triaxial test simulation reference data.

Ballast	
Ballast density (kg/m^3)	2700
Young modulus (Pa)	$5.1{\cdot}10^9$
Poisson ratio	0.18
Mean diameter (m)	0.05
Friction coefficient between stones and membrane	0.0
Friction coefficient between stones and actuators	0.268
Restitution coefficient	0.4
Membrane	
Young modulus (Pa)	$1.5{\cdot}10^6$
Poisson ratio	$1.2{\cdot}10^8$
Thickness (m)	0.0023
Penalty factor (γ)	100

Graph in Figure 5.27 shows the results obtained. It can be seen that the curve is very inclined for the first instants, reaching a value of deviatoric stress that doubles the laboratory value. When the axial strain is 3% the stress decrease and for axial strain between 3% and 5% the deviatoric stress is similar for the numerical model and the laboratory test.

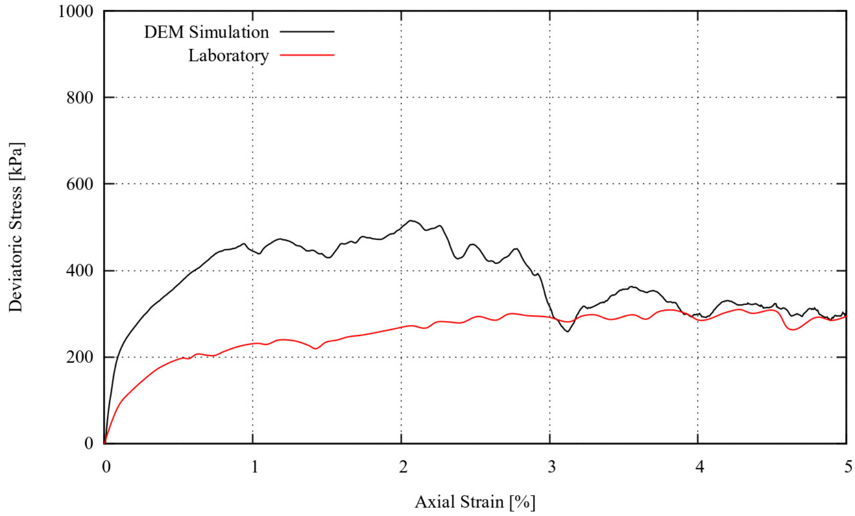

Figure 5.27: Triaxial test results.

From the graph, it can be concluded that parameters are not already well calibrated. In the initial part of the curve, when axial strain is low, ballast resistance is much higher in the simulation than in the laboratory tests. When axial strain increases (more than 3%) the difference between laboratory and numerical results decreases.

Figure 5.28 shows the membrane and ballast sample deformation before axial strain starts and after a 5% axial strain. It can be appreciated that the radial expansion of the sample is localized mainly in the top part, while the expected behaviour is radial expansion all along the sample.

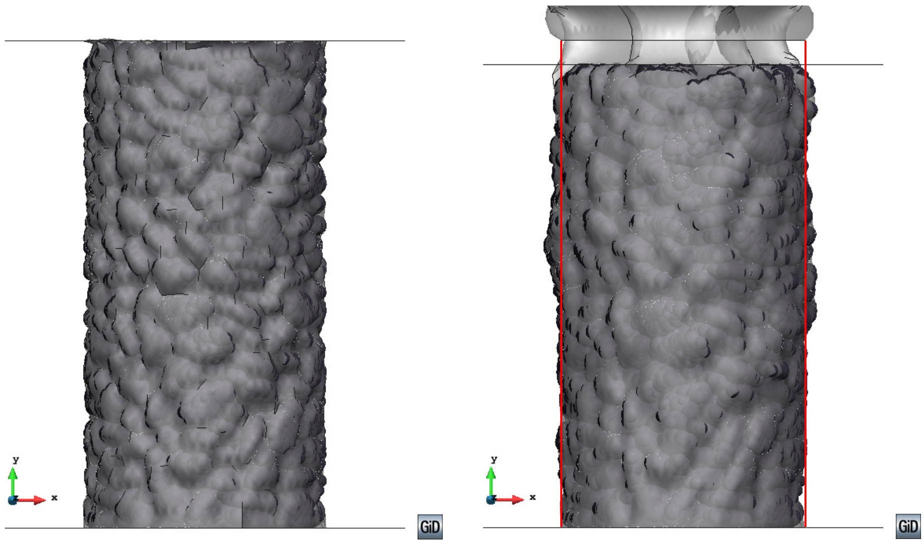

(a) Axial Strain = 0%.

(b) Axial Strain = 5%.

Figure 5.28: Triaxial test before axial strain starts (left) and after 5% axial strain (right). Red lines in the right image represent the initial width of the sample.

Although there are some similarities between numerical and laboratory results, there are also big differences between both models. One assumption that can be a source of error is the ballast friction coefficient. When representing ballast particles with clusters, the surfaces are not totally smooth, due to the overlapped spheres. This can affect the simulations, so that, a new simulation with ballast friction coefficient equal to 0.4 (instead of 0.6) is developed.

Graph of Figure 5.29 presents the results obtained with ballast friction coefficient equal to 0.4. Results improvement can be clearly seen compared with the above simulation (ballast friction coefficient 0.6).

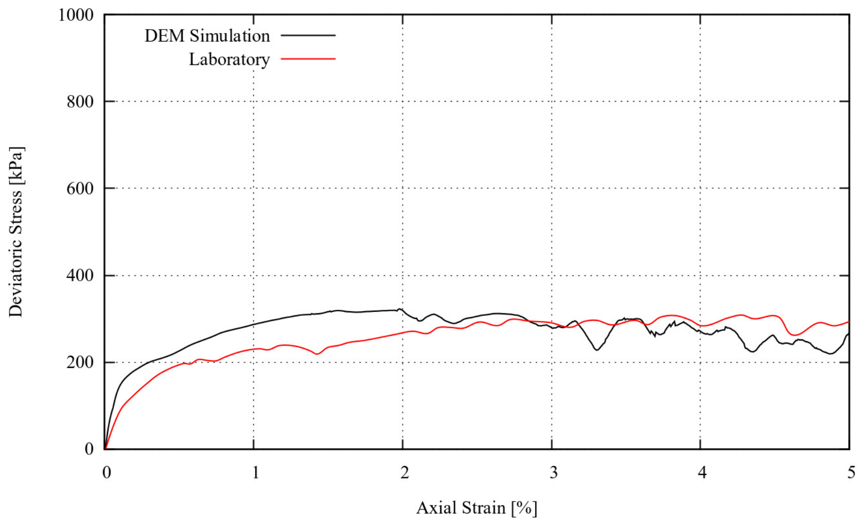

Figure 5.29: Triaxial test results with ballast friction coefficient equal to 0.4. Simulation graph finishes before 5% axial strain because the calculation is still running.

Figure 5.30 confirms results improvement, as, in this case, radial expansion occurs all along the ballast sample, not only in the top part.

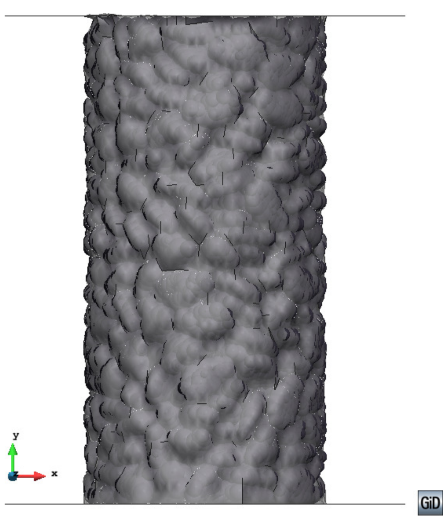

(a) Axial Strain = 0%.

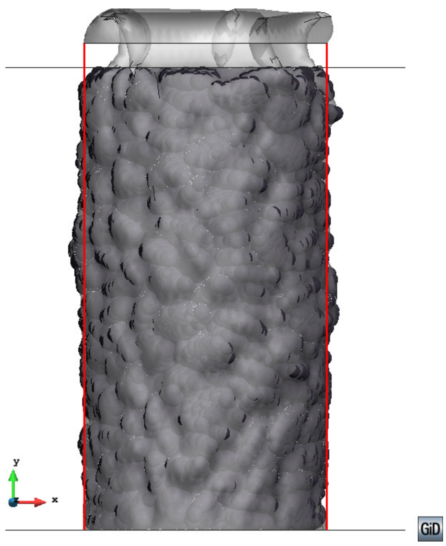

(b) Axial Strain = 5%.

Figure 5.30: Triaxial test before axial strain starts (left) and after 5% axial strain (right) for the test with ballast friction coefficient 0.4.

6 CONCLUSIONS

In this work, a brief introduction of railway infrastructures has been presented, mentioning its main characteristics, standards that should meet in Spain and new challenges appeared in the last years due to the development of high-speed trains.

Ballast aggregates is the main material used in railroad infrastructures, and DEM has been found as one of the most promising numerical methods for the calculation of granular materials. For this reason, an application (*DEM-application*) for numerical calculations using the DEM, has also been introduced.

There are some features, not already developed in the initial numerical code, that were introduced as a consequence of this research, like: rolling friction, sphere clusters generation and discrete finite element contact.

Finally two laboratory tests were simulated with the *DEM-application.* Although there are still a lot of improvements to perform, the obtained results are satisfactory and a motivation to keep working.

From all the above it can be concluded that:

- The DEM has been found as an appropriate method for the calculation of ballast aggregates. Compared with constitutive models based in continuum assumptions, DEM has the advantage of the easiness to reproduce discontinuities, anisotropy and local instabilities.
- Rolling friction, within spheric particles, seems to be useful for calculations with a great amount of material, due to the fact that particle geometry would be an approximation and also the computational cost will be smaller.
- Stiffness was not considered fundamental for the DEM calculations, as the calculation force would the same, but increasing contacts indentation. However, it has been demonstrated that for this kind of quasi-static tests it is a key property.
- Particle packing is an important variable that should be taken into account, because it greatly affects the results.
- Spheric clusters are a good approach to represent real geometries with low computational cost, but there is a drawback, the irregularities of each outer surface changes the friction coefficient. More validation work should be developed.

Finally, it should be mentioned that, although there is already too much work to do, the developed *DEM-application* is a promising tool for the calculation of ballast behaviour.

7 FUTURE WORK

The obtained results prove that the DEM is a powerful tool for the calculation of railway ballast. However, a lot of improvements could be implemented in the code, and there are also validation work to do.

Improvements to develop within the *DEM-application*:

- Create more clusters from scanned geometries.
- Find a better way to generate sphere clusters meshes, to allow more anisotropy and save time.
- Create a new *GiD problemtype*[7], specific for ballast calculations, called *DEM-Ballast*. It could be useful if it has available wizards to generate, easily, common laboratory tests (like large-scale triaxial tests).
- Develop the Central Differences algorithm (in addition to Forward Euler) for the numerical integration, as it is developed in the *Solid Mechanics application*.
- Implement particle rotation via quaternions[8], it would be more accurate than doing it in the XYZ coordinates system.

There are also some validation work to carry out:

- Evaluate the influence of clusters surface irregularities in the friction coefficient.
- Develop triaxial tests to evaluate ballast behaviour under dynamic loads.
- Simulate other laboratory tests, in addition to triaxial and lateral resistance tests. There exist other well documented laboratory tests to be simulated with the *DEM-application*. Two examples are, the ballast box test and the oedometric test [39].
- Use the Hertz constitutive model to reproduce laboratory tests, not only linear model.

[7] Problemtypes are user interface tools that can be created to facilitate the generation, using *GiD*, of *Kratos* models.

[8] Quaternions are a four-dimensions vectors that provide a convenient mathematical notation for representing orientations and rotations of objects in three dimensions

Bibliography

[1] A. Abellán Fernández. *Utilización y Validación de un Modelo de Simulación en 3D para el Cálculo de la Peligrosidad Residual por Caídas de Rocas sobre el Tren Cremallera de Vall de Núria*. Master Thesis, Universitat Politècnica de Catalunya, 2009.

[2] ADIF. Homologación de Traviesas Monobloque de Hormigón Pretensado. Technical report, 2003.

[3] N. Admetlla Pérez. *Transición Vía en Placa - Vía con Balasto Mediante Traviesas Cuadro*. Master Thesis, Universitat Politècnica de Catalunya, 2011.

[4] D. Álvarez Mántaras and P. Luque Rodríguez. *Ferrocarriles: Ingeniería e Infraestructura de los Transportes*. Universidad de Oviedo, 2003.

[5] W.F. Anderson and P. Fair. Behavior of Railroad Ballast under Monotonic and Cyclic Loading. *Journal of Geotechnical and Geoenvironmental Engineering*, 134(3):316–327, 2008.

[6] B. Aursudkij, G.R. McDowell, and A.C. Collop. Cyclic Loading of Railway Ballast under Triaxial Conditions and in a Railway Test Facility. *Granular Matter*, 11(6):391–401, 2009.

[7] N. Belheine, J.P. Plassiard, F.V. Donzé, F. Darve, and A. Seridi. Numerical Simulation of Drained Triaxial Test using 3D Discrete Element Modeling. *Computers and Geotechnics*, 36(1–2):320–331, 2009.

[8] G. Bradshaw. *Bounding Volume Hierarchies for Level-of-detail Collision Handling*. PhD thesis, Trinity College, 2002.

[9] G. Bradshaw and C. O'Sullivan. Sphere-tree Construction Using Dynamic Medial Axis Approximation. In *Proceedings of the 2002 ACM SIGGRAPH/Eurographics Symposium on Computer Animation*, SCA '02, pages 33–40, New York, NY, USA, 2002. ACM.

[10] G. Bradshaw and C. O'Sullivan. Adaptive Medial-axis Approximation for Sphere-tree Construction. *ACM Trans. Graph.*, 23(1):1–26, 2004.

[11] M.P.N. Burrow, G.S. Ghataora, and A.B.S. Stirling. A Rational Approach to Track Substructure Design. In *Proceedings of the Conference on Excellence in Railway Systems Engineering and Integration*, Derby, UK, 2005.

[12] CENIT Centro de Innovación del Transporte. Reducción de las Variaciones de Rigidez Vertical de la Vía: Establecimiento de Criterios de Diseño, Recepción y Mantenimiento de las Infraestructuras Ferroviarias. Technical report, 2008.

[13] P.W. Cleary. Large Scale Industrial DEM Modelling. *Engineering Computations*, 21(2/3/4):169–204, 2004.

[14] P.A. Cundall and O.D.L. Strack. A Discrete Numerical Model for Granular Assemblies. *Géotechnique*, 29(1):47–65, 1979.

[15] P. Dadvand. *A Framework for Developing Finite Element Codes for Multi-disciplinary Applications.* PhD thesis, Universitat Politècnica de Catalunya, 2007.

[16] Y.F. Dafalias and M.T. Manzari. A Critical State Two-surface Plasticity Model for Sands. *Géotechnique*, 47(2):255–272, 1997.

[17] J.M. Duncan. State of the Art: Limit Equilibrium and Finite-Element Analysis of Slopes. *Journal of Geotechnical Engineering*, 122(7):577–596, 1996.

[18] A. Džiugys and B. Peters. An Approach to Simulate the Motion of Spherical and Non-spherical Fuel Particles in Combustion Chambers. *Granular Matter*, 3(4):231–266, 2001.

[19] I.W. Farmer. *Engineering Properties of Rocks.* Spon, 1968.

[20] J.M. Galván Giménez. *Estudio por Elementos Finitos de la Transición Vía con Balasto - Vía en Placa.* Master Thesis, Universitat Politècnica de Catalunya, 2012.

[21] X. Garcia, J. Xiang, J.P. Latham, and J.P. Harrison. A Clustered Overlapping Sphere Algorithm to Represent Real Particles in Discrete Element Modelling. *Géotechnique*, 59(9):779–784, 2009.

[22] N. Garg and M. Thompson. Triaxial Characterization of Minnesota Road Research Project Granular Materials. *Transportation Research Record*, 1577(1):27–36, 1997.

[23] J.M. Gere and S.P. Timoshenko. *Mechanics of Materials.* Nelson Engineering, Boston, 4th edition, 1997.

[24] S. Gimeno Aribau. *Una Nueva Problemática: la Renovación de Líneas de Alta Velocidad.* Master Thesis, Universitat Politècnica de Catalunya, 2004.

[25] P.M. Hubbard. Collision Detection for Interactive Graphics Applications. *IEEE Transactions on Visualization and Computer Graphics*, 1:218–230, 1995.

[26] B. Indraratna, P.K. Thakur, and J.S. Vinod. Experimental and Numerical Study of Railway Ballast Behavior under Cyclic Loading. *International Journal of Geomechanics*, 10(4):136–144, 2010.

[27] J. Irazábal González. *Modelación Numérica del Balasto Ferroviario mediante el Método de los Elementos Discretos.* Master Thesis, Universitat Politècnica de Catalunya, 2014.

[28] K.L. Johnson. *Contact Mechanics.* Cambridge University Press, 1987.

[29] S. Johnson, J.R. Williams, and B. Cook. Contact Resolution Algorithm for an Ellipsoid Approximation for Discrete Element Modeling. *Engineering Computations*, 21(2/3/4):215–234, 2004.

[30] H. Konietzky. Numerical Modeling in Micromechanics via Particle Methods. In *International PFC Symposium*, Gelsenkirchen, Germany, 2002. CRC Press.

[31] C.A. Labra González. *Advances in the Development of the Discrete Element Method for Excavation Processes.* PhD thesis, Universitat Politècnica de Catalunya, 2012.

[32] J.P. Latham and Y. Lu. A Random Method for Simulating Loose Packs of Angular Particles Using Tetrahedra. *Géotechnique*, 51(10):871–879, 2001.

[33] J.P. Latham and A. Munjiza. The Modelling of Particle Systems with Real Shapes. *Philosophical Transactions: Mathematical, Physical and Engineering Sciences*, 362(1822):1953–1972, 2004.

[34] W.L. Lim. *Mechanics of Railway Ballast Behaviour.* PhD thesis, University of Nottingham, 2004.

[35] Z. Liu. *Measuring the Angle of Repose of Granular Systems Using Hollow Cylinders.* Master Thesis, University of Pittsburgh, 2011.

[36] A. López Pita. *Infraestructuras Ferroviarias.* Universitat Politècnica de Catalunya, 2006.

[37] A. López Pita, P.F. Teixeira, and F. Robuste. High Speed and Track Deterioration: the Role of Vertical Stiffness of the Track. In *Proceedings of the Institution of Mechanical Engineers, Part F: Journal of Rail and Rapid Transit*, volume 218, pages 31–40, 2004.

[38] M. Losada Martínez. *Curso de Ferrocarriles: Mecánica de la Vía.* Universidad Politecnica de Madrid, 1995.

[39] M. Lu. *Discrete Element Modelling of Railway Ballast.* PhD thesis, University of Nottingham, 2008.

[40] Mantenimiento de Infraestructura Renfe. Dirección Técnica/ Jefatura de vía. N.R.V. 3-1-0.0. Traviesas. Traviesas y Cachas de Madera. Technical report, 1981.

[41] Mantenimiento de Infraestructura Renfe. Dirección Técnica/ Jefatura de vía. N.R.V. 3-1-2.1. Traviesas. Traviesas Monobloque de Hormigón. Technical report, 1997.

[42] Mantenimiento de Infraestructura Renfe. Dirección Técnica/ Jefatura de vía. N.R.V. 3-1-3.1. Traviesas. Traviesas Bibloque de Hormigón. Technical report, 1999.

[43] G.R. McDowell and M. Lu. Discrete Element Modelling of Railway Ballast under Monotonic and Cyclic Triaxial Loading. *Géotechnique*, 60(6):459–467, 2010.

[44] M. Melis Maynar. *Apuntes de Introducción a la Dinámica Vertical de la Vía y a las Señales Digitales en Ferrocarriles: con 151 Programas en Matlab, Simulink, Visual C++, Visual Basic y Excel.* Ingeniería De Ferrocarriles, Metros Y Túneles, S.l., 2008.

[45] A. Munjiza. *The Combined Finite-Discrete Element Method.* Wiley, Hoboken, NJ, 1 edition edition, 2004.

[46] A. Munjiza and J.P. Latham. Comparison of Experimental and FEM/DEM Results for Gravitational Deposition of Identical Cubes. *Engineering Computations*, 21(2/3/4):249–264, 2004.

[47] G.T. Nolan and P.E. Kavanagh. Random Packing of Nonspherical Particles. *Powder Technology*, 84(3):199–205, 1995.

[48] E. Oñate and J. Rojek. Combination of Discrete Element and Finite Element Methods for Dynamic Analysis of Geomechanics Problems. *Computer Methods in Applied Mechanics and Engineering*, 193(27–29):3087–3128, 2004.

[49] E. Oñate, F. Zárate, F. Arrufat, J. Miquel, and P.A. Ubach. Modelling and Analysis of Cement and Concrete Samples under Mechanical Testing with Discrete Element Method. International Report, CIMNE, 2013.

[50] A. P. Pentland and J. R. Williams. Superquadrics and Modal Dynamics for Discrete Elements in Interactive Design. *Engineering Computations*, 9(2):115–127, 1992.

[51] Y. Qian, S.J. Lee, E. Tutumluer, Y.M.A. Hashash, D. Mishra, and J. Ghaboussi. Simulating Ballast Shear Strength from Large-Scale Triaxial Tests: Discrete Element Method. *Transportation Research Record: Journal of the Transportation Research Board*, 2374(-1):126–135, 2013.

[52] RENFE Explotaciones Forestales. Especificación Técnica para el Suministro de Traviesas y Cachas no Inyectadas, de Roble, Haya o Pino. Technical report, 1966.

[53] M. Santasusana Isach. *Continuum Modelling Using the Discrete Element Method. Theory and Implementation in an Object-oriented Software Platform.* Master Thesis, Universitat Politècnica de Catalunya, 2012.

[54] M. Santasusana Isach. *Kratos DEM, a Parallel Code for Concrete Testing Simulations using the Discrete Element Method.* Thesis proposal, Universitat Politècnica de Catalunya, 2013.

[55] J.J. Sanz Llano. *Mecánica de Suelos.* Reverte, 1975.

[56] E.T. Selig and D. Li. Track Modulus: its Meaning and Factors Influencing it. *Transportation Research Record*, (1470), 1994.

[57] Y. Song and R. Turton. Contact Detection Algorithms for DEM Simulations of Tablet-shaped Particles. *Powder Technology*, (1):32–40, 2006.

[58] A.S.J. Suiker, E.T. Selig, and R. Frenkel. Static and Cyclic Triaxial Testing of Ballast and Subballast. *Journal of Geotechnical and Geoenvironmental Engineering*, 131(6):771–782, 2005.

[59] V. Tran. *A Coupled Finite-discrete Element Framework for Soil- structure Interaction Analysis.* PhD thesis, McGill University, 2014.

[60] O. R. Walton and R. L. Braun. Simulation of Rotary-drum and Repose Tests for Frictional Spheres and Rigid Sphere Clusters. In *Presented at the 5th Joint DOE/NSF Workshop on Flow of Particulates, Ithaca, NY, 29 Sep. - 1 Oct. 1993*, 1993.

[61] P. Wriggers and C. Wellmann. *A Two-Scale Model of Granular Materials Using a Coupled DE-FE Approach.* Institut für Kontinuumsmechanik, Hannover, 2011.

[62] J. van 't Zand and J. Moraal. Ballast Resistance under Three Dimensional Loading. Technical report, Delft University of Technology, 1997.

[63] M. Zang, W. Gao, and Z. Lei. A contact Algorithm for 3D Discrete and Finite Element Contact Problems Based on Penalty Function Method. *Computational Mechanics*, 48(5):541–550, 2011.

[64] O.C. Zienkiewicz and R.L. Taylor. *The Finite Element Method for Solid and Structural Mechanics, Sixth Edition.* Butterworth-Heinemann, Amsterdam ; Boston, 6 edition edition, 2005.